
DOMAIN DECOMPOSITION OF STOCHASTIC PDEs: DEVELOPMENT OF PROBABILISTIC WIREBASKET-BASED TWO-LEVEL PRECONDITIONERS

A PREPRINT

Ajit Desai*

Department of Civil and Environmental Engineering
Carleton University
Ottawa, ON, Canada

Mohammad Khalil

Quantitative Modeling & Analysis Department
Sandia National Laboratories
Livermore, CA, United States

Chris L. Pettit

Aerospace Engineering Department
US Naval Academy
Annapolis, MD, United States

Dominique Poirer

Department of Mechanical and Aerospace Engineering
Royal Military College of Canada
Kingston, ON, Canada

Abhijit Sarkar

Department of Civil and Environmental Engineering
Carleton University
Ottawa, ON, Canada
abhijit.sarkar@carleton.ca

August 24, 2022

ABSTRACT

Realistic physical phenomena exhibit random fluctuations across many scales in the input and output processes. Models of these phenomena require stochastic PDEs. For three-dimensional coupled (vector-valued) stochastic PDEs (SPDEs), for instance, arising in linear elasticity, the existing two-level domain decomposition solvers with the vertex-based coarse grid show poor numerical and parallel scalabilities. Therefore, new algorithms with a better resolved coarse grid are needed. The probabilistic wirebasket-based coarse grid for a two-level solver is devised in three dimensions. This enriched coarse grid provides an efficient mechanism for global error propagation and thus improves the convergence. This development enhances the scalability of the two-level solver in handling stochastic PDEs in three dimensions. Numerical and parallel scalabilities of this algorithm are studied using MPI and PETSc libraries on high-performance computing (HPC) systems. Implementational challenges of the intrusive spectral stochastic finite element methods (SSFEM) are addressed by coupling domain decomposition solvers with FEniCS general purpose finite element package. This work generalizes the applications of intrusive SSFEM to tackle a variety of stochastic PDEs and emphasize the usefulness of the domain decomposition-based solvers and HPC for uncertainty quantification.

1 Introduction

The stochastic modeling of realistic problems in engineering mechanics using SSFEM may entail solving a linear (or linearized) system with millions of unknowns exploiting HPC. Domain decomposition method (DDM) can provide the necessary platform to develop fast and efficient solvers for large-scale stochastic systems for HPC [1, 2, 3, 4, 5, 6].

*Currently at the Bank of Canada

These challenges motivated Sarkar et al. [1, 2, 3, 4] to formulate and employ one-level and two-level DDM based solvers for stochastic PDEs with a few random variables. Building upon their work, the authors extended these non-overlapping DDM algorithms for a large number of random variables involving two-dimensional stochastic PDEs [5, 6].

In this paper, however, the primary attention is given to the development and efficient parallel implementation of scalable DD solvers for three-dimensional elliptic stochastic PDEs with a large number of random variables. The wirebasket-based coarse grid [7, 8] is extended to the cases of stochastic PDEs to improve the performance and scalability aspects of the DD solvers.

A large-scale system of equations arising from the application of domain decomposition algorithms to the problems in three dimensions is computationally more demanding than the problems in two dimensions. This is due to the following reasons: (a) the complex geometry of the global interface and (b) the complicated coupling among the subdomains in three dimensions.

For these reasons, the domain decomposition methods such as two-level Balancing Domain Decomposition by Constraints (BDDC) or Neumann-Neumann with a Coarse problem (NNC) and Dual-Primal Finite Element Tearing and Interconnecting (FETI-DP) with the vertex-based coarse grid are inefficient [9, 10]. The effects are more pronounced for the vector-valued PDEs in three dimensions due to complex spatial coupling among the elements of the solution vector [8, 9, 11].

Moreover, the probabilistic analysis using the intrusive polynomial chaos expansion (PCE) method adds an additional coupling structure in the resulting system of equations and further complicates the problem [4, 12]. The coupling among the PCE coefficients of the solution process and the resulting block structure of the stochastic submatrices further influence the condition number of the system resulting in SSFEM [4, 5, 12]. Therefore, the direct application of the Schur complement based two-level domain decomposition algorithms developed for two-dimensional stochastic PDEs to three-dimensional problems does not give scalable performance [4, 6].

In the cases of domain decomposition methods for stochastic PDEs in two dimensions developed earlier in [5, 6], scalable performance is achieved by providing a mechanism for global communication using vertex-based coarse grid. The coarse problem solved in the vertex-based coarse grid provides the solution only at the corner nodes (or vertices), i.e., the nodes at the ends of interface edge plus the nodes shared among three or more subdomains. The solution at the remaining interface nodes, i.e., all other interface nodes excluding vertices, is computed using the available solution at the corner nodes. In three dimensions, this procedure can introduce significant inaccuracy due to an inefficient coarse grid correction resulting from the complicated coupling among the subdomains [8, 9].

In the deterministic settings, the condition number bound for the vertex-based method in two dimensions is shown as [8, 9, 10]

$$\kappa \leq C(1 + \log(H/h))^2, \quad (1)$$

where C is a positive coefficient independent of the size of subdomains (H) and the size of element (h). These bounds are quite satisfactory in two dimensions. However, for the same method in three dimensions, the condition number bound is shown to be [8, 9, 10]

$$\kappa \leq C(H/h)(1 + \log(H/h)). \quad (2)$$

The presence of the additional multiplier (H/h) in the above equation (in contrast to Eq. (1)) leads to poor scalability in three-dimensional case.

These issues motivated Bramble [7], Smith [8], Dryja [13] and Mandel [14, 15] to work with the wirebasket-based coarse grid as shown in Fig. 1 and Fig. 2. The new coarse grid involves (a) vertices (\bullet), i.e., the nodes at the ends of interface edge plus the nodes shared among three or more subdomains and (b) the remaining nodes on the interface edge i.e., the remaining interface-edges (for brevity we omit the word nodes) (\star). Together (a) and (b) forms a wirebasket as shown in Fig. 1 and 2. The interface edge ($-$) is the boundary of the interface and the nodes on the interface edge (except vertices) are referred as interface-edges for brevity. The interface-faces (\circ) are the nodes shared between two subdomains excluding interface-edges. Note that, the interface in three dimensions is a two-dimensional having a surface defined by interface face and boundary defined by interface edge.

The wirebasket-based coarse grid can provide an efficient mechanism for global communication of information, and therefore can help in designing more efficient coarse correction procedure [8, 9, 10]. The condition number bound for the wirebasket-based approach (in the deterministic setting) is given by (refer the following articles and references therein for the theoretical proof [8, 9, 10]),

$$\kappa \leq C(1 + \log(H/h))^2. \quad (3)$$

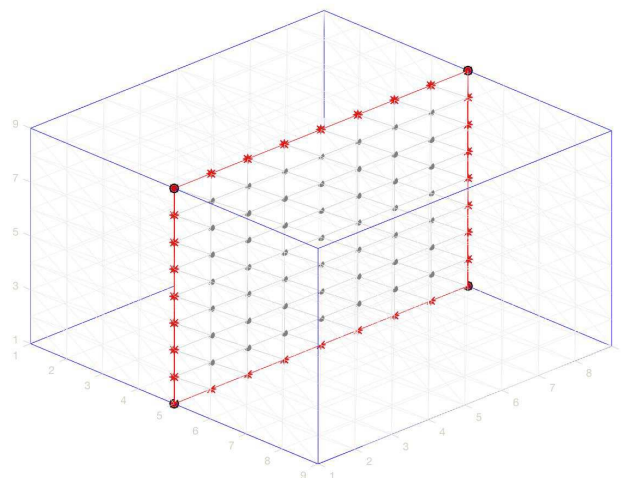
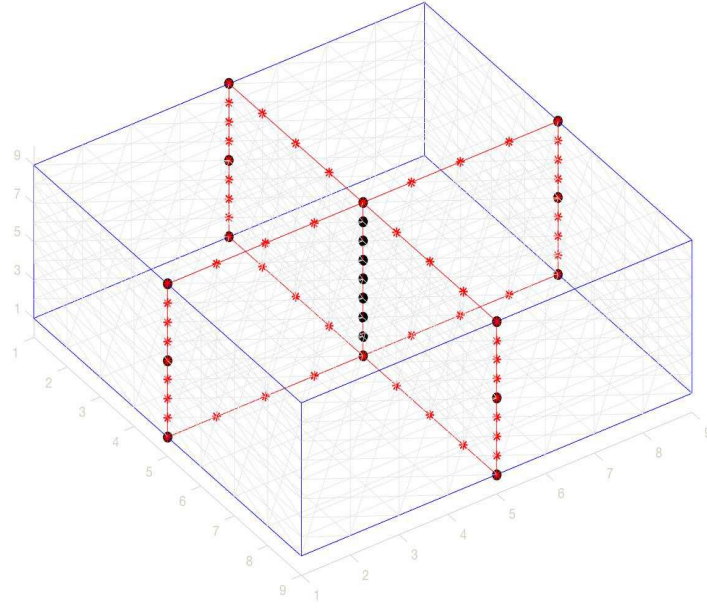


Figure 1: Schematic representation of a simple wirebasket coarse grid for a cube partitioned into two subdomains, showing (-) for the global interface edge, (•) as vertices, (*) as interface-edges and (◉) as interface-faces.

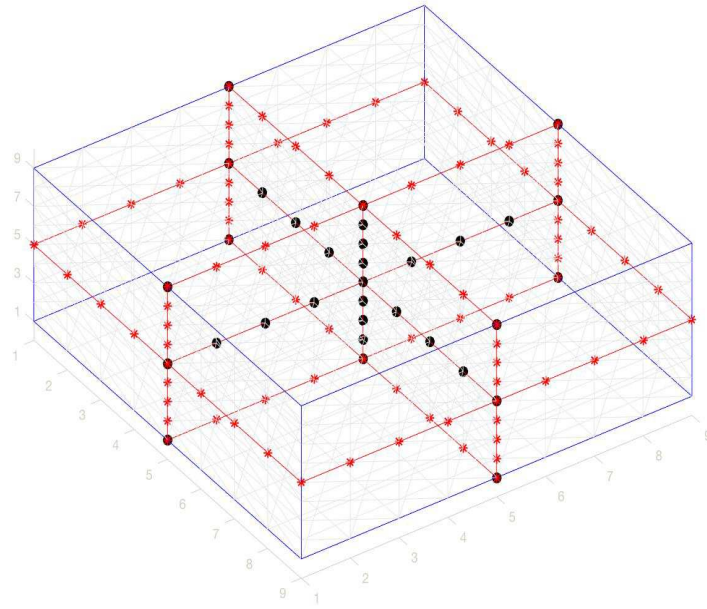
In the context of stochastic PDEs, the direct application of the vertex-based coarse grid to the problems in three dimensions result in poor scaling behavior [4]. This is due to a poorly conditioned system of equations arising in the setting of vertex-based domain decomposition methods and weak mechanism for global error propagation [4]. Moreover, the application of SSFEM further complicates the system due to the coupling among the PCE coefficients of the solution process. This results into block structure of the subdomain-level decomposed matrices, further affecting the condition number of resulting extended Schur complement system matrix [4].

Taking inspiration from the wirebasket-based approaches developed for the deterministic PDEs in three dimensions [7, 8, 10, 15], we propose the extended (to the stochastic case) wirebasket-based coarse grid with the BDDC/NNC solver for the stochastic PDEs in three dimensions. The BDDC/NNC solver with the extended wirebasket-based coarse grid is then employed to simulated large-scale, scalar and vector-valued stochastic PDEs with a large number of random variables. To this end, the contributions made in this paper are broadly categorized next.

- The extended wirebasket-based coarse grid for BDDC/NNC solver is developed to overcome the scalability issues of two-level DD solvers with the vertex-based coarse grid in three dimensions [4, 9]. The new coarse grid, which includes both vertices and interface-edges to form a wirebasket, strengthens the mechanism for global error propagation and correction, and thus improves the convergence.
- The BDDC/NNC solver with the wirebasket coarse grid is shown to outperform the vertex-based coarse grid, in regards to the numerical scalability with respect to the number of subdomains and number of random variables. The superiority of the wirebasket-based coarse grid is demonstrated for the stochastic diffusion equation and the stochastic equations of linear elasticity in three dimensions.
- Efficient implementational strategies deployed in [5, 6] are used to improve the capabilities of the wirebasket-based BDDC/NNC solver to tackle three-dimensional stochastic PDEs characterized by a large number of random variables. The three-level sparse iterative solver which employs an efficient preconditioner at each level is devised and implemented using various sparse data-structures and routines from MPI, PETSc, FEniCS and UQTK [5].
- Utilizing the subdomain-level stochastic block matrix assembly procedure presented in [6], the BDDC/NNC solver with the extended wirebasket-based coarse grid is coupled with the FEniCS deterministic finite element package [16, 17]. The coupling of BDDC/NNC solver with FEniCS reduces the implementational complexity required in the DD based intrusive SSFEM code development for the three-dimensional stochastic PDEs [18, 19, 20].
- Finally, we also present a step-by-step approach to simplify the application of intrusive SSFEM for a coupled stochastic PDE system, such as equations of linear elasticity. In such cases, the utilization of intrusive SSFEM leads to the two-levels of couplings structure, i.e., the first is due to vector-valued solution process of the



(a)



(b)

Figure 2: Schematic representation of wirebasket coarse grid for a cube partitioned into (a) four subdomains and (b) eight subdomains, showing (-) for the global interface edge, (\bullet) as vertices and (\star) as interface-edges.

coupled PDE system, and the second is due to the interdependence of PCE coefficients of the solution process. Efforts have been made to simplify the process and provide guidance to navigate such complexity.

In this paper, no attempts have been made to perform the theoretical convergence analysis and condition number bound estimation of the preconditioned extended Schur complement system in the intrusive SSFEM setting. However, extensive numerical experiments are conducted to thoroughly investigate the performance of the extended wirebasket-based BDDC/NNC solver. Modern HPC clusters (available in compute Canada [21]) are exploited to demonstrate the utility of BDDC/NNC solver with the wirebasket-based coarse grid to tackle large-scale stochastic PDEs with a large number of random variables.

First, the numerical scalability concerning the number of PCGM iterations to solve the extended Schur complement system is investigated with respect to the following: (a) increasing spatial mesh resolution with a fixed number of PCE terms, (b) increasing number of subdomains with increasing number of PCE terms for a fixed problem size per subdomains, (c) increasing number of subdomains for a fixed number of PCE terms and a fixed mesh resolution, (d) increasing number of random variables for a fixed order of expansion, and a fixed mesh resolution; and (e) increasing order of expansion for a fixed number of random variables and a fixed mesh resolution.

Secondly, the parallel scalability of the extended wirebasket-based BDDC/NNC solver is measured with respect to the strong and weak scaling [9, 22]. In the strong scalability test, the global problem size is kept constant and the number of cores used to solve the problem is increased to reduce the total execution time. For the weak scalability test, the problem size per subdomain is fixed and the global size of the problem is increased by adding more subdomains [9, 22].

Finally, the scalability study of the wirebasket-based BDDC/NNC solver concerning stochastic parameters such as the number of random variables and order of expansion is presented. The scalability of the solver with respect to stochastic parameters is crucial for uncertainty quantification. That is because, as the number of PCE terms increases, the block-sparsity structure of the underlying intrusive SSFEM system matrix changes. These effects are more substantial in the cases of the three-dimensional coupled PDE system due to the additional coupling in the spatial domain. Therefore, the scalability plots concerning stochastic parameters provide useful information regarding the effectiveness of the solver for large-scale stochastic simulations. The scalability study concerning stochastic parameters is somewhat unusual compared to the scalability studies commonly conducted for the deterministic FEM. That is because, in the deterministic setting, changing mesh density or the values of the system parameters, does not influence the block sparsity pattern of the underlying system matrix.

In the following sections, we first discuss the formulation of extended Schur complement of a coupled stochastic PDE system in Sec. 2. Next the formulation of extended wirebasket-based BDDC/NNC preconditioner for the coupled stochastic PDE system is presented in Sec. 3. This is followed by the application of extended wirebasket-based BDDC/NNC solver to the three-dimensional stochastic diffusion equation to model flow through random media in Sec. 4. The application of BDDC/NNC solver with the extended wirebasket-based coarse grid to a stochastic linear elasticity problem is presented in Sec. 5. For both stochastic Poisson and elasticity problems, the random system parameters are modeled as non-Gaussian stochastic processes characterized by using a large number of RVs (up to 15 RVs). Finally, in Sec. 6 we conclude our findings. Various algorithms demonstrating implementation of the BDDC/NNC solvers are listed in Appendix A.

2 Extended Schur Complement of Coupled Stochastic PDE System

In this section, we formulate an extended Schur complement system for a coupled stochastic PDE system. For demonstration we consider the equations of linear elasticity in three-dimensions to model the vector-valued stochastic displacement field.

The finite element discretization of a coupled stochastic PDE system defined over physical domain $\mathcal{D}(x, y, z)$ as a function of random event θ , leading to the stochastic linear system,

$$\mathbf{A}(\theta)\mathbf{u}(\theta) = \mathbf{f} \quad (4)$$

where $\mathbf{A}(\theta)$ being the stochastic coefficient matrix.

The vector-valued stochastic response field $\mathbf{u}(\theta)$ can be denoted as,

$$\mathbf{u}(\theta) = \{\mathbf{u}_x(\theta), \mathbf{u}_y(\theta), \mathbf{u}_z(\theta)\}.$$

For simplicity, the vector \mathbf{f} is considered to be a deterministic source term. However, the methodology presented here can be easily extended to the stochastic source term [23, 24].

To formulate the Schur complement system, we divide the domain \mathcal{D} into n_s non-overlapping subdomains with $s = 1, 2, \dots, n_s$. Accordingly, the subsystem for a typical subdomain s can be expressed as [4, 5],

$$\mathbf{A}^s(\theta) \mathbf{u}^s(\theta) = \mathbf{f}^s. \quad (5)$$

The local system matrix $\mathbf{A}^s(\theta)$ can be expressed in terms of the contribution from the x, y and z coordinates. Therefore, the subdomain-level stochastic equilibrium system can be expanded as

$$\begin{bmatrix} \mathbf{A}_{xx}^s(\theta) & \mathbf{A}_{xy}^s(\theta) & \mathbf{A}_{xz}^s(\theta) \\ \mathbf{A}_{yx}^s(\theta) & \mathbf{A}_{yy}^s(\theta) & \mathbf{A}_{yz}^s(\theta) \\ \mathbf{A}_{zx}^s(\theta) & \mathbf{A}_{zy}^s(\theta) & \mathbf{A}_{zz}^s(\theta) \end{bmatrix} \begin{Bmatrix} \mathbf{u}_x^s(\theta) \\ \mathbf{u}_y^s(\theta) \\ \mathbf{u}_z^s(\theta) \end{Bmatrix} = \begin{Bmatrix} \mathbf{f}_x^s \\ \mathbf{f}_y^s \\ \mathbf{f}_z^s \end{Bmatrix}. \quad (6)$$

The sparsity structure of the subdomain-level block matrix $\mathbf{A}^s(\theta)$ in Eq. (6) for a typical subdomain s , assembled at the mean values of the stochastic system parameters for the equations of linear elasticity is shown in Fig. 3.

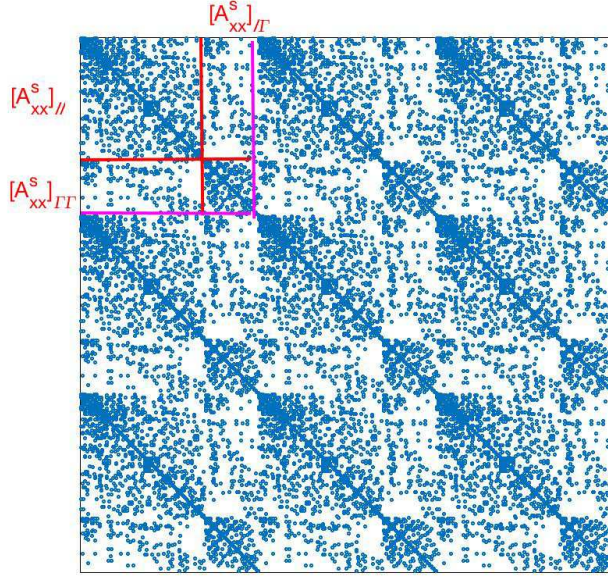


Figure 3: Subdomain-level system matrix $\mathbf{A}^s(\theta)$ computed using the mean system parameters, indicating coupling among x, y and z displacements. It also displays decomposed components for x displacements according to interior I and interface Γ nodes.

The stochastic solution vector $\mathbf{u}^s(\theta)$ for each subdomain s , has three components $\mathbf{u}_x^s(\theta)$, $\mathbf{u}_y^s(\theta)$, $\mathbf{u}_z^s(\theta)$ along spatial coordinates x, y, z respectively. Let us denote the submatrix and subvector components from Eq. (6) using $\mathbf{A}_{\alpha\beta}^s(\theta)$ and $\mathbf{u}_\alpha^s(\theta)$, where the α and β represent x, y and z components. Next, the solution vector components $\mathbf{u}_\alpha^s(\theta)$ are divided into the interior vector $(\mathbf{u}_\alpha^s)_I(\theta)$ and interface vector $(\mathbf{u}_\alpha^s)_\Gamma(\theta)$. According to this decomposition, each submatrix and subvector in Eq. (6) can be written as

$$\mathbf{A}_{\alpha\beta}^s = \begin{bmatrix} (\mathbf{A}_{\alpha\beta}^s)_{II}(\theta) & (\mathbf{A}_{\alpha\beta}^s)_{I\Gamma}(\theta) \\ (\mathbf{A}_{\alpha\beta}^s)_{\Gamma I}(\theta) & (\mathbf{A}_{\alpha\beta}^s)_{\Gamma\Gamma}(\theta) \end{bmatrix}, \quad (7)$$

$$\mathbf{u}_\alpha^s(\theta) = [(\mathbf{u}_\alpha^s)_I(\theta), (\mathbf{u}_\alpha^s)_\Gamma(\theta)]^T. \quad (8)$$

For example, see Fig. 3 which displays the decomposed matrix components $(\mathbf{A}_{\alpha\beta}^s)_{\gamma\delta}(\theta)$, according to interior and interface nodes for $\mathbf{A}_{xx}^s(\theta)$ matrix where γ and δ represent I and Γ .

The components of decomposed matrices and vectors which relate to interior nodes are given by

$$\mathbf{A}_{II}^s(\theta) = \begin{bmatrix} (\mathbf{A}_{xx}^s)_{II}(\theta) & (\mathbf{A}_{xy}^s)_{II}(\theta) & (\mathbf{A}_{xz}^s)_{II}(\theta) \\ (\mathbf{A}_{yx}^s)_{II}(\theta) & (\mathbf{A}_{yy}^s)_{II}(\theta) & (\mathbf{A}_{yz}^s)_{II}(\theta) \\ (\mathbf{A}_{zx}^s)_{II}(\theta) & (\mathbf{A}_{zy}^s)_{II}(\theta) & (\mathbf{A}_{zz}^s)_{II}(\theta) \end{bmatrix} \quad (9)$$

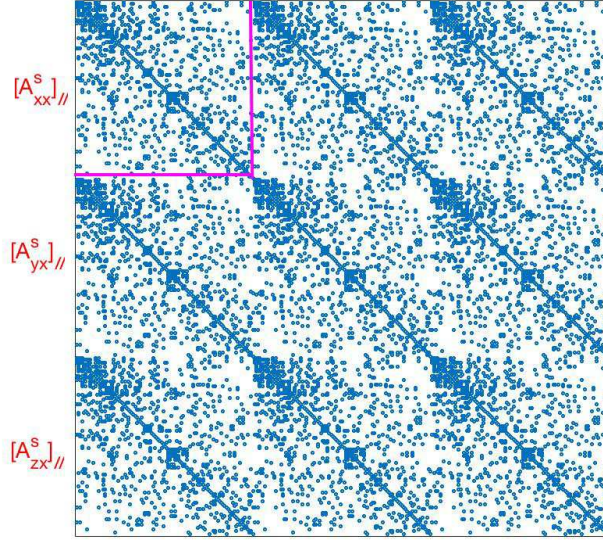


Figure 4: Subdomain-level stiffness matrix $\mathbf{A}_{II}^s(\theta)$ for interior nodes, computed using the mean system parameters, indicating coupling among x , y and z displacements.

$$\mathbf{u}_I^s(\theta) = [(\mathbf{u}_x^s)_I(\theta), [(\mathbf{u}_y^s)_I(\theta), [(\mathbf{u}_z^s)_I(\theta)]^T. \quad (10)$$

Fig. 4 displays the block matrices pertaining to interior nodes for the matrix $\mathbf{A}_{II}^s(\theta)$ as in Eq. (9).

Similar step can be taken to construct the other component matrices $(\mathbf{A}_{\alpha\beta}^s)_{\gamma\delta}(\theta)$ and vectors $(\mathbf{u}_\alpha^s)_\gamma(\theta)$. Consequently, the subsystem for a typical subdomain s can be obtained by using rearranged component matrices and vectors as,

$$\begin{bmatrix} \mathbf{A}_{II}^s(\theta) & \mathbf{A}_{I\Gamma}^s(\theta) \\ \mathbf{A}_{\Gamma I}^s(\theta) & \mathbf{A}_{\Gamma\Gamma}^s(\theta) \end{bmatrix} \begin{Bmatrix} \mathbf{u}_I^s(\theta) \\ \mathbf{u}_\Gamma^s(\theta) \end{Bmatrix} = \begin{Bmatrix} \mathbf{f}_I^s \\ \mathbf{f}_\Gamma^s \end{Bmatrix}, \quad (11)$$

where $\mathbf{u}_I^s(\theta)$ is the subdomain-level (local) interior solution vector relating to the interior nodes and $\mathbf{u}_\Gamma^s(\theta)$ is the local interface solution vector pertaining to interface nodes. The vectors \mathbf{f}_I^s and \mathbf{f}_Γ^s correspond to the source terms for interior and interface respectively.

Next, by following these steps the extended (to the stochastic case) Schur complement system is constructed as follows:

- Incorporate PCE of the stochastic system matrix blocks, $\mathbf{A}_{\gamma\delta}^s(\theta) = \sum_{i=0}^{P_A} \bar{\mathbf{A}}_{\gamma\delta,i}^s \Psi_i(\theta)$, using the P_A terms in the expansion and the stochastic solution process, $\mathbf{u}_\gamma^s(\theta) = \sum_{j=0}^{P_u} \bar{\mathbf{u}}_{\gamma,j}^s \Psi_j(\theta)$ using P_u terms in the expansion, into Eq. (11), where $\Psi_j(\theta)$ is the j^{th} PC (a known random variable) and $\bar{\mathbf{u}}_{\gamma,j}$ are unknown deterministic quantities (to be computed).
- This is followed by the Galerkin projection along the random dimension, which involves, multiplying both sides of Eq. (11) by $\Psi_k(\theta)$ with $k = \{0, 1, \dots, P_u\}$ and taking expectation.
- Enforcing the transmission conditions by performing global assembly along the interface unknowns, the following extended Schur complement system is obtained (refer to the following articles for further details [4, 5])

$$\mathbf{S}\mathbf{u}_\Gamma = \mathbf{g}_\Gamma, \quad (12)$$

\mathcal{S} being the extended Schur complement system for a coupled stochastic PDE system and \mathbf{g}_Γ is the forcing vector. They are respectively defined as

$$\mathcal{S} = \sum_{s=1}^{n_s} \mathcal{R}_s^T \left[\mathcal{A}_{\Gamma\Gamma}^s - \mathcal{A}_{\Gamma I}^s [\mathcal{A}_{II}^s]^{-1} \mathcal{A}_{I\Gamma}^s \right] \mathcal{R}_s, \quad (13)$$

$$\mathbf{g}_\Gamma = \sum_{s=1}^{n_s} \mathcal{R}_s^T \left[\mathcal{F}_\Gamma^s - \mathcal{A}_{\Gamma I}^s [\mathcal{A}_{II}^s]^{-1} \mathcal{F}_I^s \right], \quad (14)$$

where the \mathcal{R}_s denotes the restriction matrix defined later and

$$[\mathcal{A}_{\gamma\delta}^s]_{jk} = \sum_{i=0}^{P_A} \langle \psi_i \psi_j \psi_k \rangle \bar{\mathbf{A}}_{\gamma\delta,i}^s, \quad (15)$$

$$\mathbf{u}_\Gamma = [\bar{\mathbf{u}}_{\Gamma,0}, \dots, \bar{\mathbf{u}}_{\Gamma,P_u}]^T, \quad (16)$$

$$\mathcal{F}_{\gamma,k}^s = \langle \psi_k \mathbf{f}_\gamma^s \rangle. \quad (17)$$

The subdomain-level local matrices $[\mathcal{A}_{\gamma\delta}^s]_{jk}$ can be assembled by using Algorithm 2 in Appendix A.

This procedure utilizes deterministic FEniCS assembly routines, which involve manipulating element stiffness matrices to handle stochasticity (see Appendix B in [6] for further details). The structure of the local matrices $[\mathcal{A}_{\gamma\delta}^s]$ have two levels of blocks. The first-level of blocks is due to couplings among x, y and z components and the second-level of blocks is due to couplings among the PCE coefficients. These couplings produce two-levels of block-sparsity structure in each of the subdomain level decomposed matrices $[\mathcal{A}_{\gamma\delta}^s]$.

The restriction operators \mathcal{R}_s in Eq. (13) and Eq. (14) can be obtained as

$$\mathcal{R}_s = \text{blockdiagonal}(\mathbf{R}_{s,0}, \dots, \mathbf{R}_{s,P_u}), \quad (18)$$

where each of the blocks (with $i = \{0, 1, \dots, P_u\}$) can be obtained as

$$\mathbf{R}_{s,i} = \text{blockdiagonal}(\mathbf{R}_s^{x,i}, \mathbf{R}_s^{y,i}, \mathbf{R}_s^{z,i}). \quad (19)$$

The $\mathbf{R}_s^{\alpha,i}$ in eq. (19) (where α denotes x, y or z) manages gather or scatter operations as follows,

$$(\mathbf{u}_{\alpha,i}^s)_\Gamma = [\mathbf{R}_s^{\alpha,i}] (\mathbf{u}_{\alpha,i})_\Gamma, \quad (20)$$

$$(\mathbf{u}_{\alpha,i})_\Gamma = [\mathbf{R}_s^{\alpha,i}]^T (\mathbf{u}_{\alpha,i}^s)_\Gamma. \quad (21)$$

The matrix components, $\mathcal{A}_{\gamma\delta}^s$ in Eq. (13) and (14) (where γ and δ representing I or Γ) are considerably larger, complex and computationally intensive to assemble compared to $A_{\gamma\delta}^s$ for scalar-valued stochastic PDEs [6]. To simplify assembly procedure for stochastic matrix $\mathcal{A}_{\gamma\delta}^s$, FEniCS-based deterministic assembly routines are employed. The probabilistic Schur complement system in Eq. (12) for a stochastic PDE system is more complex and computationally expensive compared to the extended Schur complement system obtained in the case of scalar-valued stochastic PDEs [6].

For deterministic PDEs the solution of extended Schur complement system using two-level preconditioner with vertex-based coarse grid does not give scalable performance [4]. Therefore, the wirebasket-based coarse grid is required to overcome this challenge [8, 9]. Therefore the probabilistic two-level preconditioner using extended wirebasket for stochastic PDE system is presented in the next section.

3 Two-Level Preconditioner using Extended Wirebasket-Based Coarse Grid for SPDEs

Two-level preconditioner with a coarse problem is required to achieve scalable performance with DD-based iterative solvers [4, 25]. To overcome the scalability issues of vertex-based coarse grid, we propose extended wirebasket-based coarse grid with the two-level BDDC/NNC preconditioner for SPDEs.

The wirebasket, as shown in Fig. 1, includes the interface edges (nodes on the edges of the boundary \star) along with the vertices (the nodes at the end of the interface plus the nodes shared by three or more subdomains \bullet). The wirebasket

can provides an efficient mechanism for global error propagation during each iteration of BDDC/NNC based PCGM solver of the extended Schur complement system shown in Eq. (12). The formulation of extended wirebasket-based BDDC/NNC preconditioner for SPDEs is briefly discussed below.

The local interface unknowns \mathcal{U}_F^s (for each subdomain s) are partitioned into faces \mathcal{U}_F^s and wirebasket \mathcal{U}_W^s such that

$$\begin{Bmatrix} \mathcal{U}_F^s \\ \mathcal{U}_W^s \end{Bmatrix} = \begin{Bmatrix} \mathcal{R}_s^F \\ \mathcal{R}_s^W \end{Bmatrix} \mathcal{U}_\Gamma^s, \quad (22)$$

where the restriction operators are obtained as,

$$\mathcal{R}_s^F = \text{blockdiagonal}(\mathbf{R}_{s,0}^F, \dots, \mathbf{R}_{s,P_u}^F), \quad (23)$$

$$\mathcal{R}_s^W = \text{blockdiagonal}(\mathbf{R}_{s,0}^W, \dots, \mathbf{R}_{s,P_u}^W). \quad (24)$$

The P_u is the number of PCE terms used in the characterization of solution process. The $\mathbf{R}_{s,i}^\gamma$ blocks in Eq. (23) and (24) where γ represents F or W and $i = \{0, 1, \dots, P_u\}$ are represented by the component matrices as follows:

$$\mathbf{R}_{s,i}^F = \text{blockdiagonal}(\mathbf{R}_{s,i}^{Fx}, \mathbf{R}_{s,i}^{Fy}, \mathbf{R}_{s,i}^{Fz}), \quad (25)$$

$$\mathbf{R}_{s,i}^W = \text{blockdiagonal}(\mathbf{R}_{s,i}^{Wx}, \mathbf{R}_{s,i}^{Wy}, \mathbf{R}_{s,i}^{Wz}). \quad (26)$$

The components $\mathbf{R}_{s,i}^{\gamma\delta}$ (with δ represents x, y or z), acts as a gather or scatter operator between local faces/wirebasket and global faces/wirebasket components of the deterministic interface solution vectors.

Accordingly the global coarse problem arising in the setting of BDDC/NNC preconditioner is (refer to [4, 5] for detailed procedure to construct coarse problem),

$$\mathcal{F}_{WW} \mathcal{U}_W = \mathcal{d}_W, \quad (27)$$

where \mathcal{U}_W denotes global wirebasket unknowns, \mathcal{F}_{WW} is the coarse operator and \mathcal{d}_W is corresponding right-hand side vector, being expressed as

$$\mathcal{F}_{WW} = \sum_{s=1}^{n_s} \mathcal{B}_W^s \mathcal{T} \left(\mathcal{S}_{WW}^s - \mathcal{S}_{WF}^s [\mathcal{S}_{FF}^s]^{-1} \mathcal{S}_{FW}^s \right) \mathcal{B}_W^s, \quad (28)$$

$$\mathcal{d}_W = \sum_{s=1}^{n_s} \mathcal{B}_W^s \mathcal{T} \left(f_W^s - \mathcal{S}_{WF}^s [\mathcal{S}_{FF}^s]^{-1} f_F^s \right), \quad (29)$$

where $\mathcal{S}_{\alpha\beta}^s = \mathcal{A}_{\alpha\beta}^s - \mathcal{A}_{\alpha I}^s [\mathcal{A}_{II}^s]^{-1} \mathcal{A}_{I\beta}^s$, where α and β represent W or F .

The \mathcal{B}_W^s is the restriction operator that maps the global wirebasket unknowns to local wirebasket unknowns. The \mathcal{B}_W^s can be obtained as,

$$\mathcal{B}_W^s = \text{blockdiagonal}(\mathbf{B}_{W,0}^s, \dots, \mathbf{B}_{W,P_u}^s), \quad (30)$$

where each block (with $i = \{0, 1, \dots, P_u\}$) can be obtained as

$$\mathbf{B}_{W,i}^s = \text{blockdiagonal}(\mathbf{B}_{W,x,i}^s, \mathbf{B}_{W,y,i}^s, \mathbf{B}_{W,z,i}^s). \quad (31)$$

and $\mathbf{B}_{W,\alpha,i}^s$ relates the global and local corner node solutions as:

$$(\mathbf{u}_{\alpha,i}^s)_W = [\mathbf{B}_{W,\alpha,i}^s] (\mathbf{u}_{\alpha,i})_W. \quad (32)$$

where α represents x, y and z .

Performing algebraic manipulations, the two-level BDDC/NNC preconditioner with the wirebasket-based coarse grid can be written as (refer [4, 5] for further details),

$$\mathcal{M}_{NNW}^{-1} = \sum_{s=1}^{n_s} \mathcal{R}_s^T \mathcal{D}_s (\mathcal{R}_s^F \mathcal{T} [\mathcal{S}_{FF}^s]^{-1} \mathcal{R}_s^F) \mathcal{D}_s \mathcal{R}_s + \mathcal{R}_0^T [\mathcal{F}_{WW}]^{-1} \mathcal{R}_0. \quad (33)$$

The \mathcal{R}_0 in Eq. (33) relates global fine grid and coarse grid components [4, 5], as given by

$$\mathcal{R}_0 = \sum_{s=1}^{n_s} \mathcal{B}_W^s \mathcal{T} (\mathcal{R}_s^W - \mathcal{S}_{WF}^s [\mathcal{S}_{FF}^s]^{-1} \mathcal{R}_s^F) \mathcal{D}_s \mathcal{R}_s, \quad (34)$$

where \mathcal{D}_s is a diagonal scaling operator obtained as follows,

$$\mathcal{D}_s = \text{blockdiagonal}(\mathcal{D}_{s,0}, \dots, \mathcal{D}_{s,P_u}) \quad (35)$$

where $\mathcal{D}_{s,i}$ are obtained by using deterministic diagonal scaling matrices $\mathcal{D}_{s,i}^\alpha$ as,

$$\mathcal{D}_{s,i} = \text{blockdiagonal}(\mathcal{D}_{s,i}^x, \mathcal{D}_{s,i}^y, \mathcal{D}_{s,i}^z). \quad (36)$$

where $i = \{0, 1, \dots, P_u\}$ and α represent x , y and z .

From Eq. (33), it can be noted that the extended wirebasket-based BDDC/NNC preconditioner consists of two operators. First, the local-fine operator $(\mathcal{R}_s^{F^T} [\mathcal{S}_{FF}^s]^{-1} \mathcal{R}_s^F)$, requires a local solve $[\mathcal{S}_{FF}^s]^{-1}$ on each of the subdomains for each PCGM iteration for interface-face nodes. Second, the global coarse operator $\mathcal{R}_0^T [\mathcal{F}_{WW}]^{-1} \mathcal{R}_0$, involves a global coarse problem solve $[\mathcal{F}_{WW}]^{-1}$ for each PCGM iteration for the wirebasket nodes. This coarse operator provides an efficient mechanism for global error propagation during each application of preconditioner, therefore, accelerates the convergence of the PCGM solver [8, 9, 26].

In this following sections, we utilize the extended wirebasket-based coarse grid presented in this section to solve both scalar and vector-valued stochastic PDEs in three-dimensions. We first consider steady-state stochastic diffusion equation in three-dimensions to model the scalar-valued stochastic solution process. This is followed by the solutions of the equations of linear elasticity in three-dimensions having stochastic parameters.

4 Three-Dimensional Poisson Problem

We consider a three-dimensional stochastic diffusion problem with a spatially varying random diffusion coefficient. The flow is modeled by a three-dimensional Poisson problem having a spatially varying stochastic diffusion coefficient c_d on a domain \mathcal{D} defined as:

$$-\nabla \cdot (c_d(\mathbf{x}, \theta) \nabla \mathcal{U}(\mathbf{x}, \theta)) = F(\mathbf{x}), \quad \mathcal{D} \times \Omega, \quad (37)$$

$$\mathcal{U}(\mathbf{x}, \theta) = 0, \quad \delta\mathcal{D} \times \Omega, \quad (38)$$

where ∇ being the gradient operator, $F(\mathbf{x})$ and \mathcal{U} are the forcing and solution vectors respectively, and θ denotes the random dimension [27].

The lognormal stochastic process, $l(\mathbf{x}, \theta) = \exp(g(\mathbf{x}, \theta))$ defines the diffusion coefficient c_d with the underlying Gaussian process $g(\mathbf{x}, \theta)$ having a mean μ , variance σ^2 and the exponential covariance function C defined as [4, 24],

$$C(x_1, y_1, z_1; x_2, y_2, z_2) = \sigma^2 e^{-|x_2-x_1|/b_x - |y_2-y_1|/b_y - |z_2-z_1|/b_z}, \quad (39)$$

where b_x , b_y and b_z are the correlation lengths along x , y and z directions respectively.

For simplicity, we consider deterministic source term $F(\mathbf{x}) = 1$. The correlation lengths $b_x = b_y = b_z = 1$ and standard deviation $\sigma = 0.3$ are used to characterize the underlying Gaussian process. Numerical experiments are performed for the three-dimensional computational domain shown in Fig. 5 which depicts a typical unstructured finite element mesh with 31598 nodes and 182681 linear (four node) tetrahedral elements partitioned into 320 subdomains.

Similar to the two-dimensional cases, we primarily focus on the scalabilities of the solver to tackle the high-dimensional stochastic systems. Various simulations are conducted with increasing number of random variables. We begin with the numerical experiments in Sec. 4.1, followed by the discussion on the characteristics of the solution process in Sec. 4.2. Next, in Sec. 4.3, we compare the scalability plots for the extended wirebasket-based coarse grid with the vertex-based coarse grid. Finally, in Sec. 4.4, we present the numerical and parallel scalability plots for the wirebasket-based BDDC/NNC solvers.

4.1 Numerical Experimental Framework

The PCGM Algorithm 1 presented in Appendix A is utilized to implement NCC/BDDC solver with the extended wirebasket-based preconditioner presented in Sec. 3. The solver is implemented by using Fortran programming language. Parallel computation is managed by Message Passing Interface (MPI) communication routines [28] in conjunction with PETSc [29] for local (subdomain-level) sparse matrix vector operations, GMSH [30, 31] for mesh generation along with METIS graph partitioner [32, 33]. Stochastic system matrix and vector assembly is performed by employing element-level (deterministic) assembly routines from the FEniCS/dolfin finite element software [16]. UQ Toolkit [34] routines are used for computations relevant to KLE and PCE entities. ParaView [35, 36] and Matlab [37] are employed for post processing and visualization.

The simulations are performed on Canada's national HPC clusters managed by Compute Canada [21]. The nodes employed have either Intel Skylake cores running at 2.4 GHz from Niagara supercomputer [38] or Intel E5-2683 processors, running at 2.1 GHz from Cedar and Graham HPC systems [21].

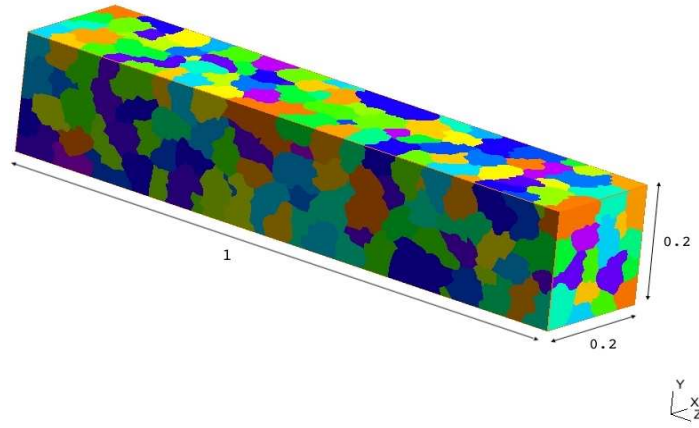


Figure 5: A typical three-dimensional finite element mesh partitioned into 320 subdomains.

4.2 Characteristics of the Solution Process

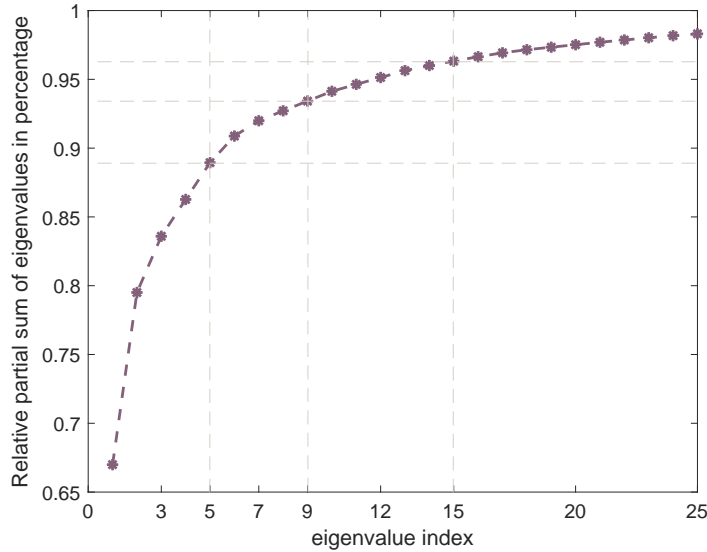


Figure 6: Relative partial sum of eigenvalues with respect to eigenvalue-index.

As a test case, consider five random variables ($L = 5$) and the second order expansion ($p_A = 2$) for the PCE of the input stochastic process. Using 5 RVs we can capture about 89% percent of the relative energy contribution for the given stochastic process. The relative energy contribution or the decay rate of the eigenvalues determines the number of random variables required in the KLE to approximate the underlying Gaussian process. For instance, using 9 RVs we can capture about 94% percent of the relative energy contribution and using 15 RVs we can capture about 97% of the relative energy contribution. See Fig. 6 for the relative partial sum of eigenvalues for the respective eigenvalue index [4, 24].

The PCE of the solution process with the five random variables ($L = 5$) and the third order expansion $P_u = 3$ is used. For these parameters, we used 21 PCE terms to approximate the input stochastic process and 56 PCE terms to approximate the output stochastic process [24].

The resulting linear system is solved for the solution PCE coefficients using the in-house parallel BDDC/NNC solvers with wirebasket-based coarse grid discussed earlier in Sec. 3.

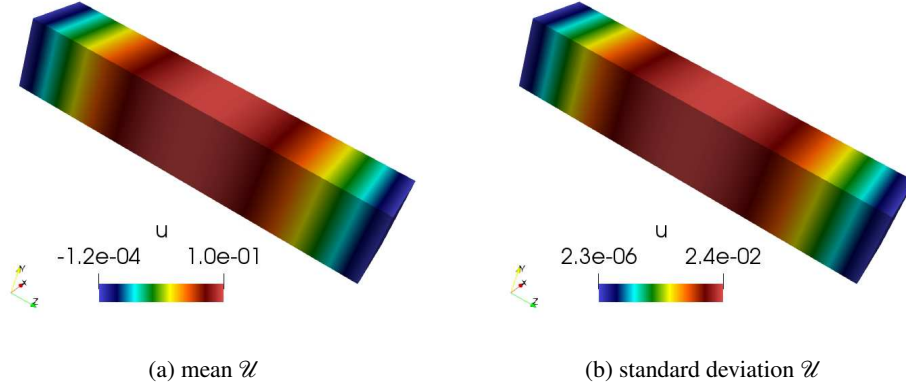


Figure 7: Mean and standard deviation of the solution process \mathcal{U} .

The mean and standard deviation of the solution field \mathcal{U} has the same trend, but, of course, their magnitudes are different. See Fig. 7 (a) and (b) respectively showing mean and standard deviation (SD) of the solution process. The maximum coefficient of variation in the centre of the domain is about 25%. To get the further insights into the stochastic aspects of the solution process, the first few PCE coefficients are plotted in Figs. 8 to 10. One can see that, the PC coefficients exhibit oscillatory behavior and the magnitude of the chaos coefficients u_j decreases with increasing PCE index j . Among these PCE coefficients, the first order coefficients contain Gaussian contributions and the higher order coefficients contain the non-Gaussian effects. As the order of expansion increases, the mean and standard deviation of the solution process converge as shown in Fig. 7.

4.3 Comparison of Extended Wirebasket-based and Vertex-based Algorithms

The performance of extended wirebasket-based coarse grid preconditioner devised earlier is compared to that of the extended vertex-based coarse grid. In the current investigation, we primarily focus on to the performance comparison concerning numerical scalabilities of the solvers,

i.e., the number of PCGM iterations necessary for the convergence with the given tolerance:

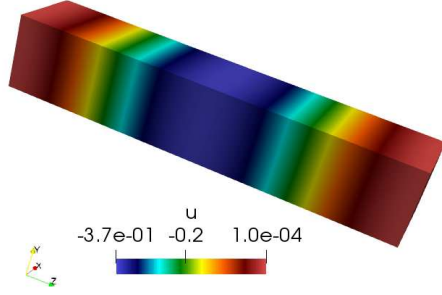
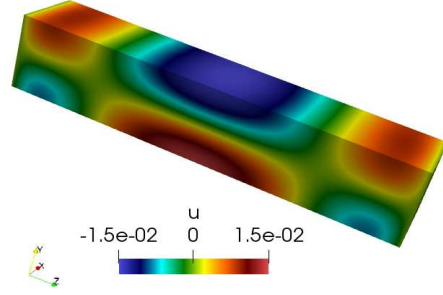
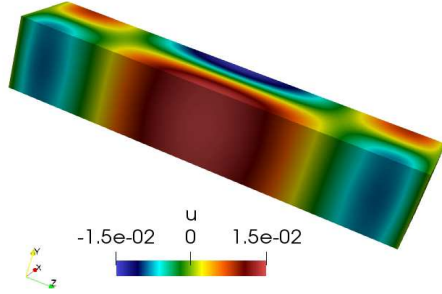
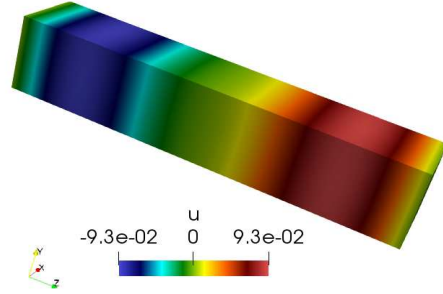
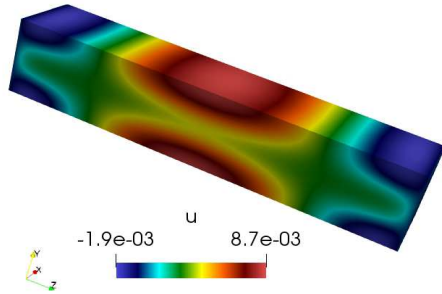
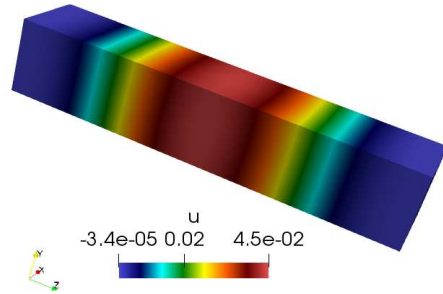
$$\frac{\|\mathcal{U}_{\Gamma_{i+1}} - \mathcal{U}_{\Gamma_i}\|_2}{\|\mathcal{U}_{\Gamma_i}\|_2} \leq tol = 10^{-5},$$

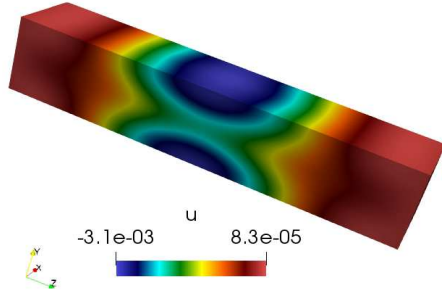
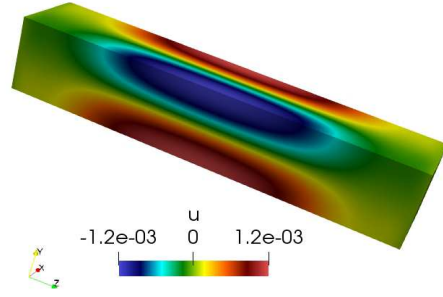
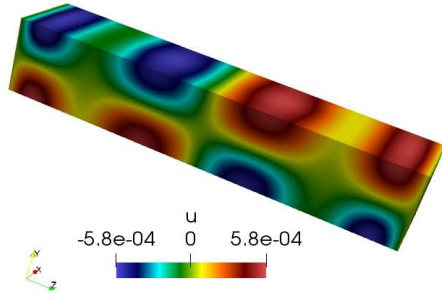
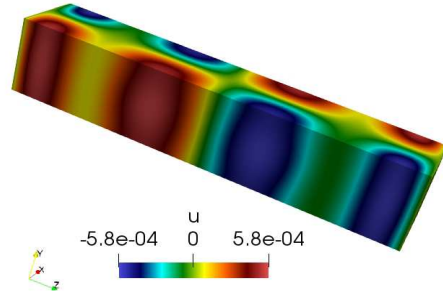
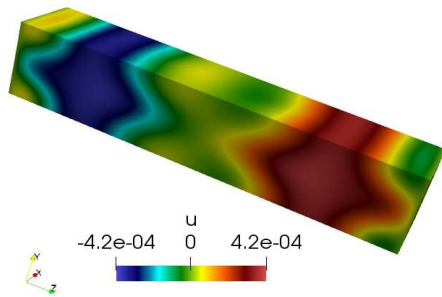
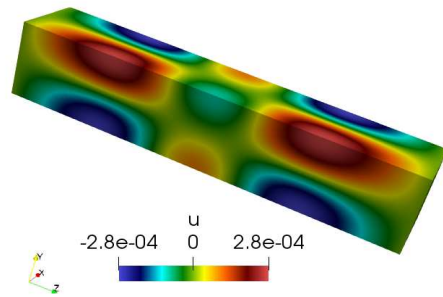
where $\|\cdot\|_2$ represents the L_2 norm and the subscript i indicating the PCGM iteration number.

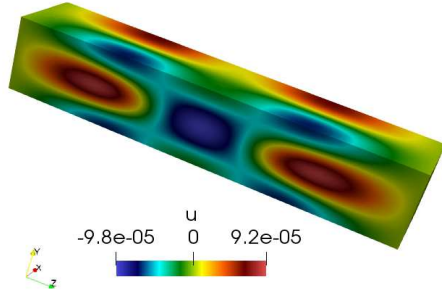
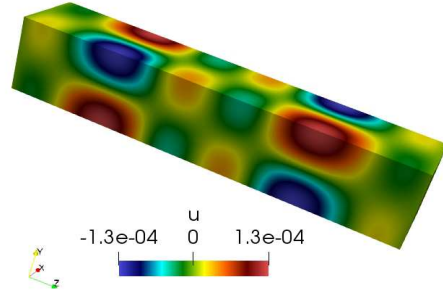
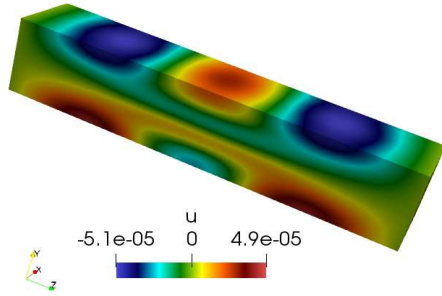
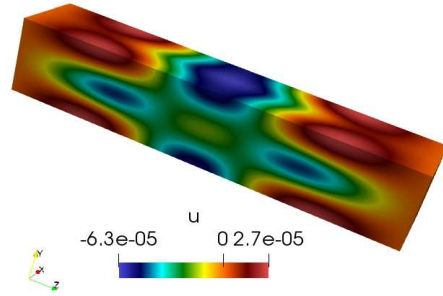
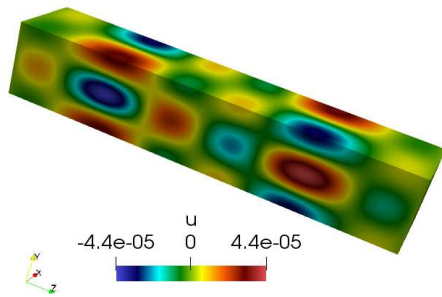
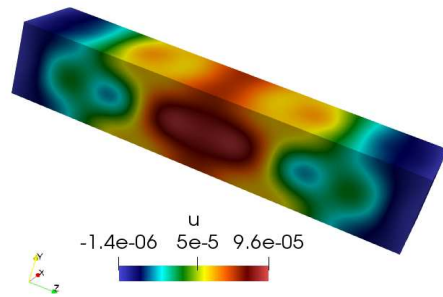
The numerical scaling is essential to understanding the convergence behavior of the solver. Therefore the numerical scalability is considered crucial for the utility of the solver for the large-scale applications. Note that, the finite element mesh with the fixed resolution having 31598 nodes and 182681 (linear tetrahedral) elements is used for all simulations in this section. The maximum size of the linear system tackled in this section is about ≈ 7 million, i.e., 31598 nodes \times 220 PCE terms.

For a fixed mesh resolution and the fixed PCE terms ($P_u = 56$), and increasing number of subdomains (accordingly number of cores), the number of PCGM iteration increases faster with the vertex-based coarse grid compared to that of the wirebasket-based coarse grid. The BDDC/NNC solver with wirebasket-based coarse grid showed better numerical scaling with respect to the number of subdomains compared to the vertex-based coarse grid (Fig. 11).

For a fixed mesh resolution, the global problem size relates to the number of PCE terms (i.e., $P_u = 20, 56, 120$ and 220 , corresponding to $L = 3, 5, 6$ and 9 , respectively). For roughly the fixed problem size per core (≈ 15000), the resulting linear system is tackled using more cores. For the fixed problem size per core, the PCGM iteration count for the wirebasket-based preconditioner against subdomain counts remains almost the same (Fig. 12). On the other hand, for the same case, the number of iterations increases with the vertex-based coarse grid. Therefore, the wirebasket-based coarse grid BDDC/NNC solver scales better with respect to the number of PCE terms compared to the vertex-based

(a) PCE coefficient u_1 (b) PCE coefficient u_2 (c) PCE coefficient u_3 (d) PCE coefficient u_4 (e) PCE coefficient u_5 (f) PCE coefficient u_6 Figure 8: Selected PCE coefficients of the solution process \mathcal{U} .

(a) PCE coefficient u_{10} (b) PCE coefficient u_{12} (c) PCE coefficient u_{13} (d) PCE coefficient u_{16} (e) PCE coefficient u_{19} (f) PCE coefficient u_{27} Figure 9: Selected PCE coefficients of the solution process \mathcal{U} .

(a) PCE coefficient u_{32} (b) PCE coefficient u_{41} (c) PCE coefficient u_{45} (d) PCE coefficient u_{48} (e) PCE coefficient u_{50} (f) PCE coefficient u_{53} Figure 10: Selected PCE coefficients of the solution process \mathcal{U} .

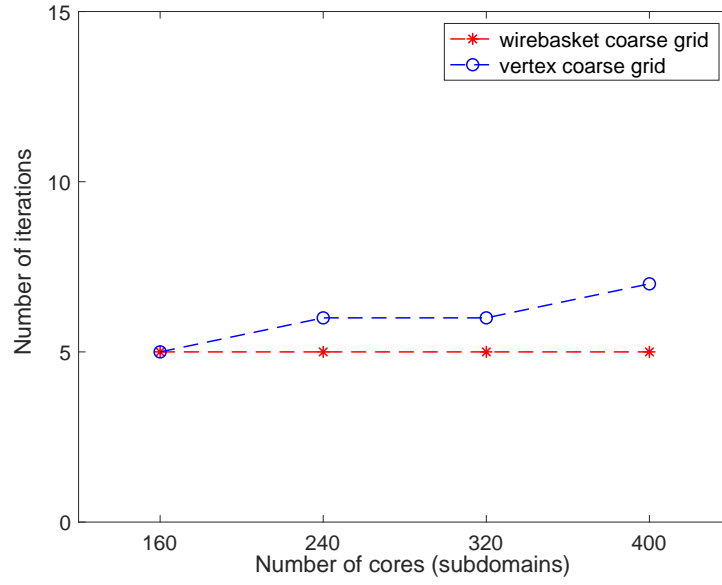


Figure 11: Iteration count versus number of subdomains for the fixed mesh resolution with fixed number of PCE terms.

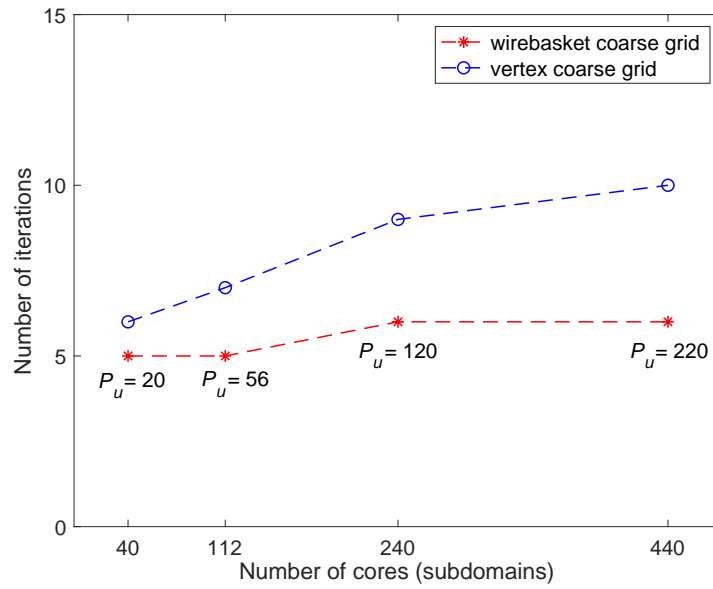


Figure 12: Number of iterations versus number of subdomains for fixed problem size per subdomain with increasing number of PCEs (fixed mesh resolution).

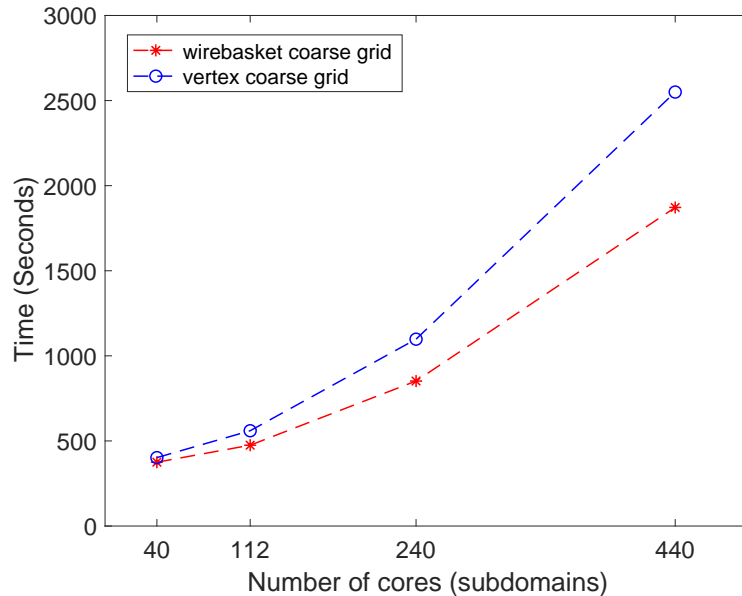


Figure 13: Execution time versus number of subdomains for increasing number of PCEs with fixed problem size per subdomain (fixed mesh resolution).

coarse grid. For the same case as in Fig. 12, the total execution time for the wirebasket-based coarse grid and vertex-based coarse grid BDDC/NNC solvers against the number of subdomains (with the fixed problem size per subdomain) are compared in Fig. 13. Total execution time for the BDDC/NNC solver with the vertex-based coarse grid increases faster compared to that of the wirebasket-based coarse grid. This is primarily due to more PCGM iteration required with the vertex-based coarse grid.

For a fixed mesh and number of subdomains ($n_s = 384$), the PCGM iteration counts for the wirebasket-based preconditioner remain nearly constant against increasing PCE terms (by adding more random variables, but with the third-order expansion) as shown in Fig. 14. Conversely, for the same case, the number of PCGM iterations increases with the vertex-based coarse grid. Therefore, the BDDC/NNC solver with the extended wirebasket-based coarse grid is superior to vertex-based coarse grid concerning numerical scaling with respect to the number of subdomains and the number of random variables.

4.4 Scalabilities Studies for Stochastic Simulations

Next we investigate the performance of the proposed wirebasket-based preconditioner for high dimensional stochastic space. Therefore, for most of the simulations, the fixed mesh with 59741 nodes and 350113 elements is used. For some cases, the mesh size is increased up to 159193 nodes and 947046 elements.

The scalability plots for various cases by selecting the number of random variables ranging between 3 to 12 are presented. The relative contribution of the KLE eigenvalues is used to select these cases (see Fig. 6).

The orders of expansion $p_A = 2$ and $p_u = 3$ are used for the input and output PCE representations, respectively. Note that the orders of expansion, p_A and p_u are kept constant for most of the experiments.

For some cases p_u is varied between 2 to 5. The number of solution PCE terms varies from 20 to 455 [24]. The maximum size of the system of linear equations simulated in this case is about 75 million, i.e., using finite element mesh with approximately 160 thousand node points and 455 PCE terms (12-RVs). To test the numerical scalability of the solver, we study the PCGM iterations counts for the convergence with the tolerance $tol = 10^{-5}$.

Next, we analyze the (strong and weak) parallel scalabilities in terms of execution time against the number of subdomains. Finally, we present the numerical and parallel scalability plots with respect to the stochastic parameters such as the number of random variables and the order of expansion.

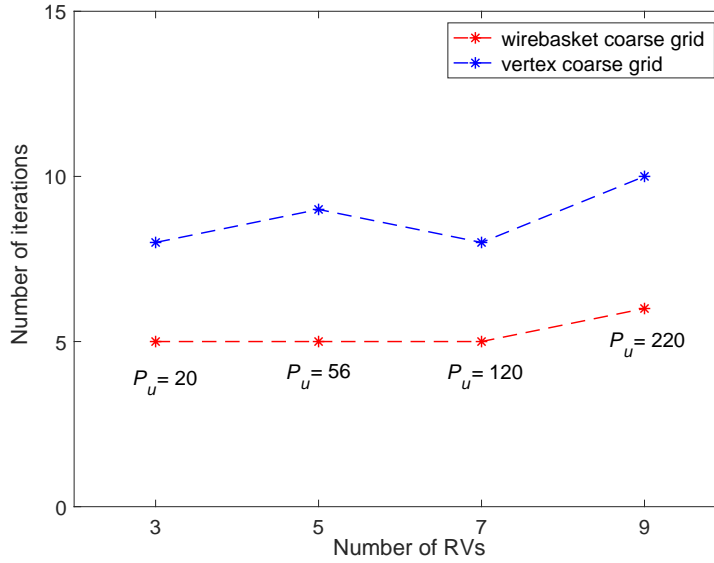


Figure 14: Iteration count versus number PCE terms for the fixed mesh resolution with fixed number of subdomains.

4.4.1 Numerical Scalability

For a fixed problem size (59741 nodes and 350113 elements and PCE terms $P_u = 120$ for 7 RVs), the PCGM iteration count almost remains constant with increasing the number of subdomains indicating the numerical scalability of the wirebasket-based BDDC/NNC-PCGM solver (Fig. 15).

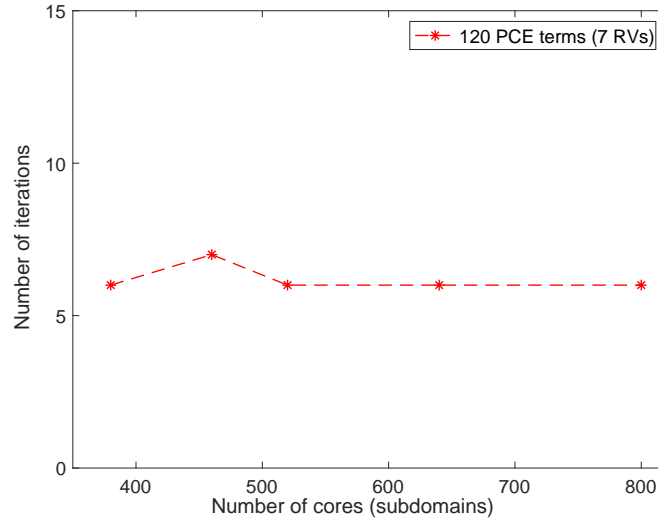


Figure 15: Iteration count versus number of subdomains for the fixed number of PCE terms and the fixed mesh resolution.

Next, for the fixed number of PCE terms ($P_u = 56$ for 5 RVs), the global problem size is increased by increasing mesh resolution for a fixed problem size per subdomain (≈ 10500). As the sizes of the total problem and coarse problem increase while adding new subdomains, the PCGM iteration count increases moderately with subdomain counts. Fig. 16 shows reasonable numerical scalability of BDDC/NNC-PCGM solver with respect to mesh resolution and fixed problem size per subdomain.

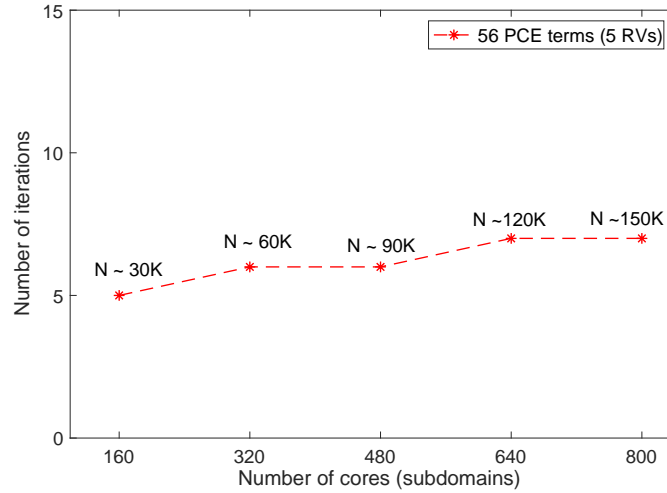


Figure 16: Iteration count versus number of subdomains for the fixed problem size per core with increasing mesh resolution (fixed number of PCE terms).

4.4.2 Parallel Scalabilities

Fig. 17 shows the strong scaling plots of the BDDC/NNC-PCGM solver. For the fixed number of PCE terms ($P_u = 120$ for 7 RVs) and a fixed spatial mesh resolution, increasing core counts cut the execution time as expected. Fig. 17 indicates excellent strong scaling of the BDDC/NNC solver with the wirebasket-based coarse grid. Similar behavior is observed in the cases with three and five random variables (although not shown here).

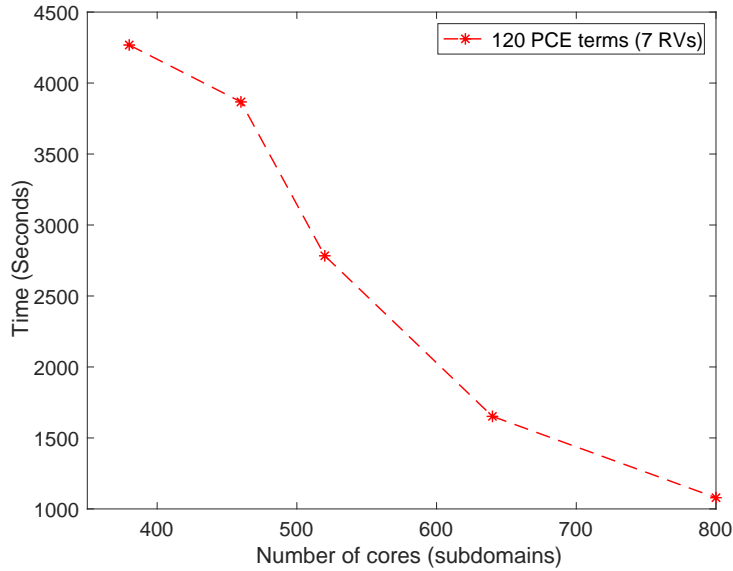


Figure 17: Execution time versus number of subdomains with the number of PCE terms and the fixed mesh resolution.

The weak scaling of the wirebasket-based solver is shown in Fig. 18. For the fixed number of PCE terms ($P_u = 56$ for 5 RVs), the global problem size is increased by increasing mesh resolution while keeping a fixed problem size per subdomain (≈ 10500). The growth in the total execution time implies that the probabilistic BDDC/NNC solver shows poor weak scaling. Similar behavior is also observed in the cases of probabilistic BDDC/NNC solver for the

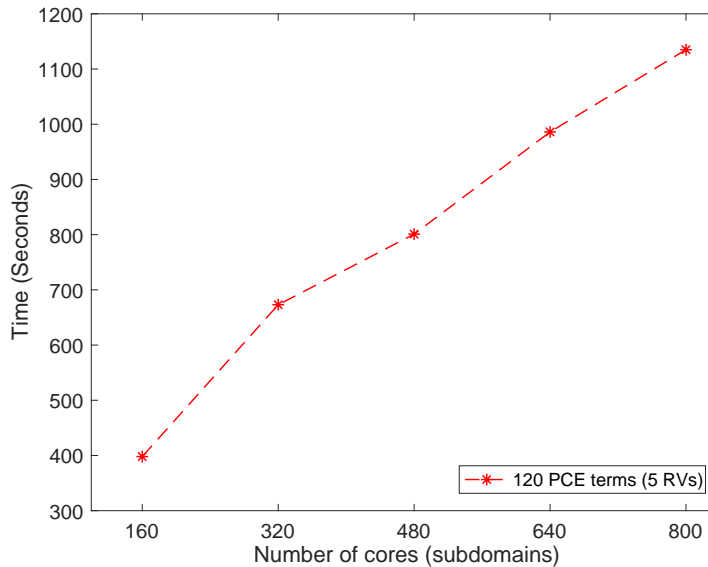


Figure 18: Execution time versus number of subdomains for the fixed problem size per core with increasing mesh resolution (fixed number of PCE terms).

two-dimensional stochastic diffusion equations [6]. The suboptimal weak scaling of the solver is mainly because of the increased parallel overhead with the number of cores caused by the MPI collective communication [4, 5]. The wirebasket coarse problem increases substantially with the number of subdomains, demanding more computational efforts.

4.4.3 Scalability with respect to Stochastic Parameters

To study the stochastic aspect of the solver, the numerical and parallel scaling against PCE terms and the order of expansions are presented in this section. The four points in Figs. 19 to 21 for PCE terms 20, 56, 120 and 220 correspond to the input random variables 3, 5, 7 and 9 respectively, with the mesh having 59741 nodes and 350113 elements.

For a fixed mesh and subdomains ($n_s = 640$), an increase in the number of PCE terms by only increasing the number of random variables, i.e., maintaining the fixed order of expansion, requires almost constant PCGM iterations (Fig. 19). This demonstrates that, a larger problem due to increasing PCE terms can be tackled with nearly constant PCGM iteration counts. This fact demonstrates the numerical scalability of the wirebasket-based BDDC/NNC-PCGM solver against the number of random variables.

Fig. 20 demonstrates that the wirebasket-based BDDC/NNC-PCGM solver's numerical scalability with respect to the number of PCE terms. For a fixed mesh, the larger linear system with increasing PCE terms is solved by adding more cores, maintaining approximately the same problem size per core (≈ 15000). In this case, The PCGM iteration counts against the number of subdomains (with the fixed problem size per subdomain) remain nearly the same.

For the third order output PCE expansion with 3, 5, 7 and 9 RVs, Fig. 21 shows the execution time of the solver for a fixed problem size per subdomain. The increase in the execution time is primarily due to increased MPI collective communication overhead. Additionally, as pointed out earlier in [6], the increasing PCE terms leads to a larger set of coupled PDEs with a more complex coupling structure.

For a fixed mesh with fixed number of subdomains ($n_s = 800$), while maintaining the fixed number of random variables $L = 5$, an increase in the number of PCE terms by increasing the order of expansion p_u , results in almost constant PCGM iteration counts (Fig. 22). It suggests the numerical scalability of the solver against the order of PCE expansion. Note that, the coupling structures resulting from increasing number of PCE terms by increasing the number of random variables are more complex and computationally demanding than those resulting from increasing order of expansion [6].

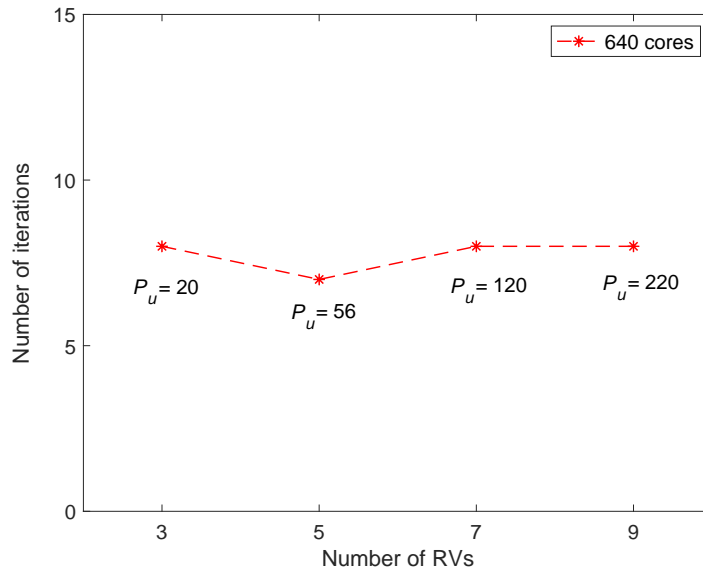


Figure 19: Iteration count versus number PCE terms for the fixed mesh resolution with fixed number of subdomains.

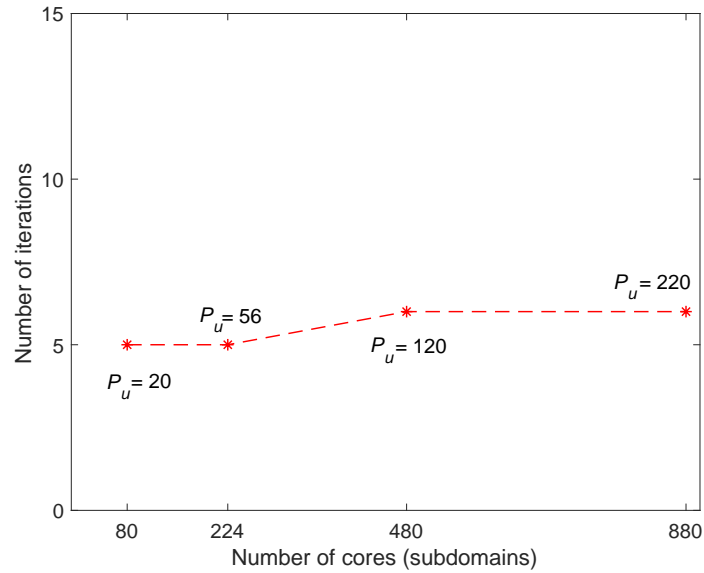


Figure 20: Iteration count versus number of subdomains for the fixed problem size per core with increasing number of PCE terms (fixed mesh resolution).

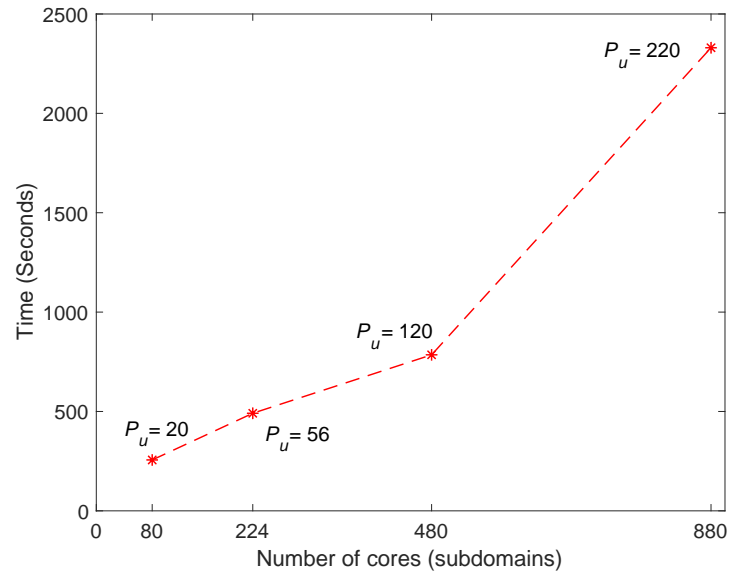


Figure 21: Execution time versus number of subdomains for fixed problem size per subdomain with increasing number of PCEs (fixed mesh resolution).

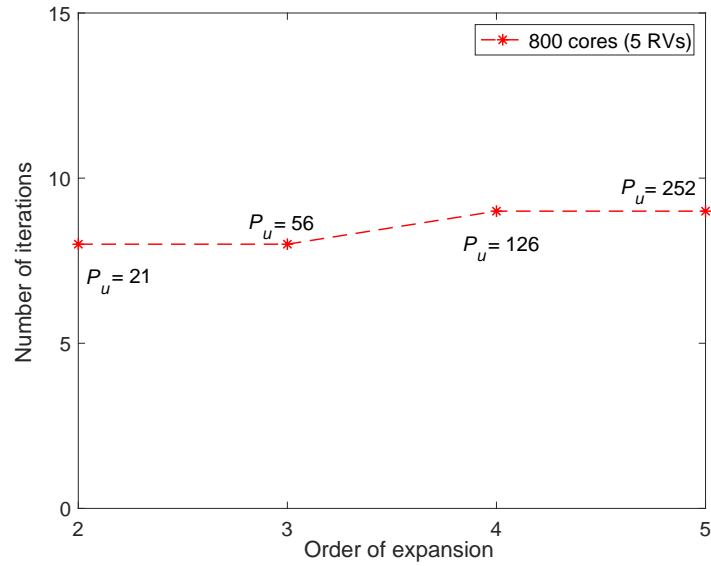


Figure 22: Iteration count versus order of expansion for the fixed mesh resolution with fixed number of subdomains (fixed number of RVs).

5 Three-Dimensional Linear Elasticity Problem

Application of deterministic finite element method to the equations of linear elasticity results in an extremely large, coupled system of linear equations for high resolution meshes. This linear system is often much more computationally expensive than those resulting from finite element discretization of scalar-valued elliptic PDEs, such as diffusion equation [9, 10]. Therefore solution of such system demands extensive computational efforts [9, 10, 11]. Moreover, extending the problem in stochastic space by using polynomial chaos expansion based intrusive SSFEM adds an additional coupling in the resulting system of equations and further complicates the system [4]. This coupling among the polynomial chaos coefficients of the vector-valued solution process results in complicated block structure of the stochastic system matrix. Therefore, this can further influence the condition number of the global Schur complement system resulting from non-overlapping domain decomposition method. To tackle such system, a simple vertex-based coarse grid is inefficient [4], as we need a much stronger mechanism such as a wirebasket coarse grid to communicate information globally [4, 11]. In this section, we employ the two-level BDDC/NNC preconditioner using extended wirebasket-based coarse grid discussed in Sec. 3, to simulate the stochastic system of coupled equations in linear elasticity.

To simplify the application of DD-based intrusive SSFEM to a coupled stochastic PDE system, we have presented a detailed formulation for the extended Schur complement system for coupled stochastic PDE system in Sec. 2. The efforts are made to explain the two-levels of couplings arising in the setting of DD-based intrusive SSFEM due to PC expansion of vector-valued solution process. In Sec. 5.1, an experimental framework for the numerical simulations of a cantilever beam is discussed. This is followed by the discussion on the characteristics of the stochastic solution process in Sec. 5.2. The Sec. 5.3 is dedicated to comparing the numerical scalability of BDDC/NNC solver with the extended wirebasket-based coarse grid against the vertex-based coarse grid. Finally in Sec. 5.4, the numerical and parallel scalability results of wirebasket-based BDDC/NNC solver are presented for a cantilever beam deformed due to self-weight.

In this section, we exploit extended wirebasket-based BDDC/NNC preconditioners to solve the Schur complement system for a coupled stochastic PDE system exemplified through linear elasticity problems. For an exposition of the methodology, we consider the equations of linear elasticity to model the vector-valued stochastic displacement field $\mathbf{U}(\mathbf{x}, \theta)$ of a three-dimension body defined over the volume $\mathcal{D}(x, y, z)$. The resulting equations can be written as [8, 9, 11],

$$-\nabla \cdot \sigma(\mathbf{U}(\mathbf{x}, \theta)) = F(\mathbf{x}) \quad \text{in } \mathcal{D}, \quad (40)$$

$$\sigma(\mathbf{U}(\mathbf{x}, \theta)) \cdot \hat{\mathbf{n}} = b_T \quad \text{on } \Gamma_1 = \delta\mathcal{D} \setminus \Gamma_0, \quad (41)$$

$$\mathbf{U}(\mathbf{x}, \theta) = 0 \quad \text{on } \Gamma_0, \quad (42)$$

where σ is the stress tensor, F is the body force vector per unit volume, $\hat{\mathbf{n}}$ is the outward unit normal on the boundary Γ and b_T is the traction on the boundary Γ_1 . For homogeneous and isotropic linear elasticity the stress tensor σ can be written as [9, 16]

$$\sigma(\mathbf{U}(\mathbf{x}, \theta)) = \lambda(\nabla \cdot \mathbf{U}(\mathbf{x}, \theta))I + 2\mu\epsilon, \quad (43)$$

where I is the identity matrix, the μ and λ are Lamé constants and ϵ is the symmetric strain tensor expressed by

$$\epsilon = \frac{1}{2}(\nabla \mathbf{U}(\mathbf{x}, \theta) + (\mathbf{U}(\mathbf{x}, \theta))^T). \quad (44)$$

To construct the variational form we take

inner product of Eq. (40) with the test function \mathbf{V} and integrate over the domain \mathcal{D} ,

$$\int_{\mathcal{D}} (-\nabla \cdot \sigma(\mathbf{U})) \cdot \mathbf{V} dx = \int_{\mathcal{D}} F \cdot \mathbf{V} dx. \quad (45)$$

Integrating by parts, Eq. (45) becomes (note \mathbf{x} and θ of \mathbf{U} are dropped for brevity),

$$\int_{\mathcal{D}} \sigma(\mathbf{U}) : \nabla \mathbf{V} dx = \int_{\mathcal{D}} F \cdot \mathbf{V} dx + \int_{\Gamma_1} b_T \cdot \mathbf{V} ds, \quad (46)$$

where the operator $:$ is the inner product between tensors. b_t is prescribed on a part Γ_1 of the boundary. Therefore, the integral on the remaining part of the boundary Γ_0 vanishes due to a Dirichlet boundary condition. Eq. (46) can be re-written more concisely using *bilinear* and *linear forms* as,

$$a(\mathbf{U}, \mathbf{V}) = \mathcal{L}(\mathbf{V}). \quad (47)$$

Lamé constants arising in the stress-strain relationship for the material can be written as the functions of Poisson ratio ν and Young's modulus E as follows [9, 16],

$$\lambda = \frac{E\nu}{(1+\nu)(1-2\nu)}, \quad \mu = \frac{E}{2(1+\nu)}. \quad (48)$$

For simplicity, we consider Poisson's ratio as a spatially invariant parameter and model Young's modulus as the lognormal stochastic process representing spatially varying uncertainty,

$$E(\mathbf{x}, \theta) = E_0(\mathbf{x})\exp(g(\mathbf{x}, \theta)), \quad (49)$$

where $E_0(\mathbf{x})$ represents the mean and $g(\mathbf{x}, \theta)$ denotes the underlying Gaussian process with the variance σ^2 and the exponential covariance function C defined as [4, 24].

$$C(x_1, y_1, z_1; x_2, y_2, z_2) = \sigma^2 e^{-|x_2-x_1|/b_x - |y_2-y_1|/b_y - |z_2-z_1|/b_z}, \quad (50)$$

where b_x , b_y and b_z are the correlation lengths along x , y and z directions respectively. While the assumption of the spatial invariance on the Poisson's ratio simplifies the analysis, the spatial variability of both Poisson's ratio and Young's modulus can be handled concurrently as the proposed framework is general [24, 39, 40].

5.1 Numerical Experimental Framework

For the extended wirebasket-based BDDC/NNC solver, the PCGM presented in Algorithm 1 [6] is implemented using Fortran programming language with MPI communication routines [28].

Subdomain-level sparse matrix-vector storage, operations and local system solves are implemented using PETSc [29]. GMSH [31] is used for unstructured finite element mesh generation and METIS graph partitioner [33] is used for mesh partitioning. The stochastic system matrix and vector assemblies are performed by employing element-level (deterministic) assembly routines from the FEniCS/dolfin [16]. The KLE and PCE related computations are performed using the UQ Toolkit [34]. ParaView [35, 36] and Matlab [37] are employed for post processing and visualization. The simulations are performed on Canada's national HPC clusters managed by Compute Canada [21]. The nodes employed have either Intel Skylake cores running at 2.4 GHz from Niagara supercomputer [38] or Intel E5-2683 processors, running at 2.1 GHz from Cedar and Graham HPC systems [21]. Similar to the earlier cases, the primary attention is given to study the efficacy of the NNC/BDDC solver in tackling high-dimensional coupled stochastic systems. In all the simulations we use (four node) linear tetrahedral elements. Such low order linear finite elements are shown to be sufficient for compressible elastic materials [41, 42]. In the following sections, we will briefly discuss the characteristics of the solution process and, numerical and parallel scalabilities of the solver by varying the number of random variables.

5.2 Characteristics of the Solution Process

As a test case, consider a clamped beam of length L_b with a square cross section of width W , deformed under self-weight in three dimensions. A typical finite element mesh for such beam with 31598 nodes and 182681 linear tetrahedral elements and 320 subdomains (see Fig. 23).

For the numerical experiments we have used the nondimensionalized and scaled system parameters suggested in FEniCS tutorial [16]. The parameters are made dimensionless by using beam length and $\mathcal{U} = \mathcal{U}/\mathcal{U}_m$. The scaling is achieved by choosing \mathcal{U}_m equal to the maximum deflection of a clamped beam (refer to FEniCS tutorial [16] for further details). The advantage of using scaled problem is to reduce the need for setting the physical parameters and also, the obtained dimensionless numbers can be used to understand the competition of parameters and physical effects. Furthermore, the dimensionless parameters simplify the computational model and make it ideal for numerical experiments. The following values are used for numerical simulations (as suggested in FEniCS tutorial [16]); Lamé constants are fixed to $\mu = 1$ and $\lambda = 1.25$. The density of the beam is set to $\rho = 1$ and the acceleration due to gravity is set to $g = 0.4(W/L_b)^2$. The beam is deformed under its weight with $F = (0, -\rho g, 0)$, where F is the body force per unit volume and the boundary Γ_1 is traction free, i.e., $b_T = 0$.

For simplicity, we assume a constant Poisson's ratio $\nu = 0.2778$ and model Young's modulus E to be a non-Gaussian process representing spatially varying uncertainty as shown in Eq. (49). The $E_0 = 2.556$ is calculated from Eq. (48) using $\mu = 1$ and $\lambda = 1.25$. Young's modulus, represented as a lognormal stochastic process, is derived from the underlying Gaussian process with zero mean, 0.3 standard deviation and exponential covariance kernel with the correlation lengths $b_x = b_y = b_z = 1$. The PCE of the input stochastic process is represented using three random variables ($L = 3$) and the second order expansion ($p_a = 2$). The PCE of the solution process with $L = 3$ and $p_u = 3$ is used. For the selected L and p_α , we need 10 PCE terms for the input and 20 PCE terms for the output [4]. The mean value

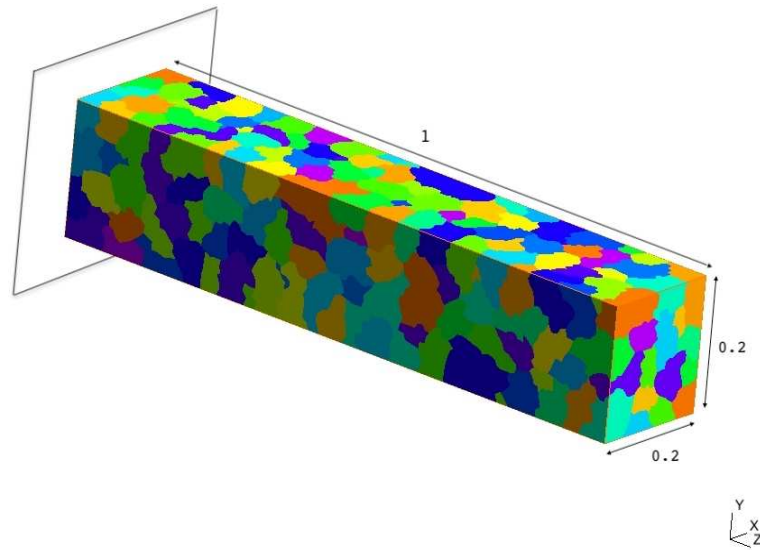


Figure 23: A typical three-dimensional finite element mesh for a clamped beam partitioned into 320 subdomains.

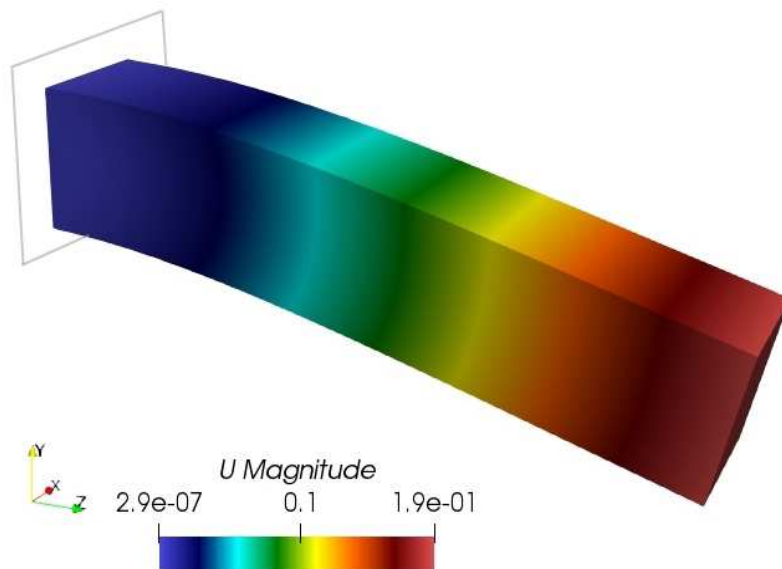


Figure 24: Mean magnitude of the beam deflection subjected to self-weight.

of the magnitude of the deflected beam is shown in Fig. 24. As expected, the maximum deflection occurs at the tip. The maximum coefficient of variation in the displacement magnitude is about 26%, highlighting the effect of input uncertainty. The mean and standard deviation (SD) of the magnitude of \mathbf{u} and its components u_x , u_y and u_z are shown in Fig. 25. The magnitude of the mean and SD have the same trend but the components of the displacement vector exhibit more complicated features. The mean of the magnitude of deflection at the mid-span and the free end of the beam approximately matches with the analytical solution obtained at the mean values of the system parameters.

To get further insights into the stochastic aspects of the solution process, the first few PCE coefficients showing the magnitude and the respective displacement components of the solution process are plotted in Figs. 26 to 29. Similar to the earlier observation, the contribution of the chaos coefficients u_j to the solution process decreases with increasing PCE index j . Among these coefficients, the first order coefficients contain Gaussian contributions and the higher order coefficients contain the non-Gaussian effects. When the PCE terms increase, the solution mean and standard deviation converge as shown in Fig. 25.

5.3 Comparison of Extended Wirebasket with Vertex Coarse Grid

The performance of the extended wirebasket-based coarse grid preconditioner is compared to the extended vertex-based coarse grid to tackle the stochastic PDE system in linear elasticity. We focus on the numerical scalabilities of the solvers, i.e., the PCGM iteration count for convergence with a tolerance:

$$\frac{\|\mathbf{u}_{\Gamma_{i+1}} - \mathbf{u}_{\Gamma_i}\|_2}{\|\mathbf{u}_{\Gamma_i}\|_2} \leq tol = 10^{-5},$$

where the subscript denotes iteration number.

For a fixed mesh resolution, i.e., 31598 nodes and 182681 (four node) linear tetrahedral elements, with a fixed number of PCE terms ($P_u = 56$ for 5 RVs), the PCGM iteration count grows quickly with the number of subdomains for the vertex-based coarse grid. The growth of the iteration count with the wirebasket-based coarse grid is smaller compared to that of the vertex-based coarse grid. Fig. 30 suggests that the BDDC/NNC solver with wirebasket-based coarse grid showed superior numerical scaling with respect to the number of subdomains compared to the vertex-based coarse grid. For a fixed mesh resolution (20753 nodes and 119179 linear tetrahedral element), the global problem size grows with increasing number of PCEs by changing the number of RVs $L = 2, 3, 5$ and 7.

The resulting larger system is tackled by adding more cores, maintaining the problem size per core ≈ 22500 . The iteration count for the wirebasket-based solver increases slightly with the subdomain numbers as shown in Fig. 31. On the other hand, for the same case, the number of iterations grows quickly with the vertex-based coarse grid. Therefore, the BDDC/NNC solver with the wirebasket-based coarse grid is superior to the vertex-based coarse grid regarding the numerical scalability against the PCE terms.

For the same case as in Fig. 31, the run time for the wirebasket-based solver and vertex-based solver against the subdomain counts (with the fixed problem size/core) are compared in Fig. 32. The execution time for the vertex-based solver increases faster than the wirebasket-based solver. This is primarily due to more PCGM iteration required with the vertex-based coarse grid.

For a fixed mesh (31598 nodes and 182681 linear tetrahedral element) and a fixed subdomain ($n_s = 400$), increasing PCE terms by adding more random variables (while maintaining the third-order expansion), results in a small increase in the PCGM iteration counts for the case with the wirebasket-based coarse grid, as shown in Fig. 33. Conversely, for the same case, the PCGM iteration count increases faster with the vertex-based coarse grid. Therefore, the BDDC/NNC solver with the extended wirebasket-based coarse grid is superior to vertex-based coarse grid for numerical scaling against the output PCE terms (due to increasing input RVs).

5.4 Scalabilities Studies for Stochastic Simulations

Next we study the performance of the wirebasket-based BDDC/NNC solver in high dimensional stochastic space. Therefore, for most of the simulations, a fixed mesh (with 48563 nodes and 283886 elements) is used. For some cases, the mesh size is increased up to 89657 nodes and 523450 elements. The performance plots include the number of random variables ranging from 2 to 9. The relative contribution of the KLE eigenvalues to the total energy (variance) of the signal guides the selection of these cases (see Fig. 6).

The orders of expansion $p_A = 2$ and $p_u = 3$ are used for the input and output PCE representations, respectively. Note that the orders of expansion, p_A and p_u are kept constant for most of the experiments. For some cases p_u is varied between 2 to 4; resulting in 20 to 220 PCE output terms [24]. The maximum linear system size handled is about 60 million, i.e., using finite element mesh with approximately 90,000 node points and 220 PCE terms (9-RVs).

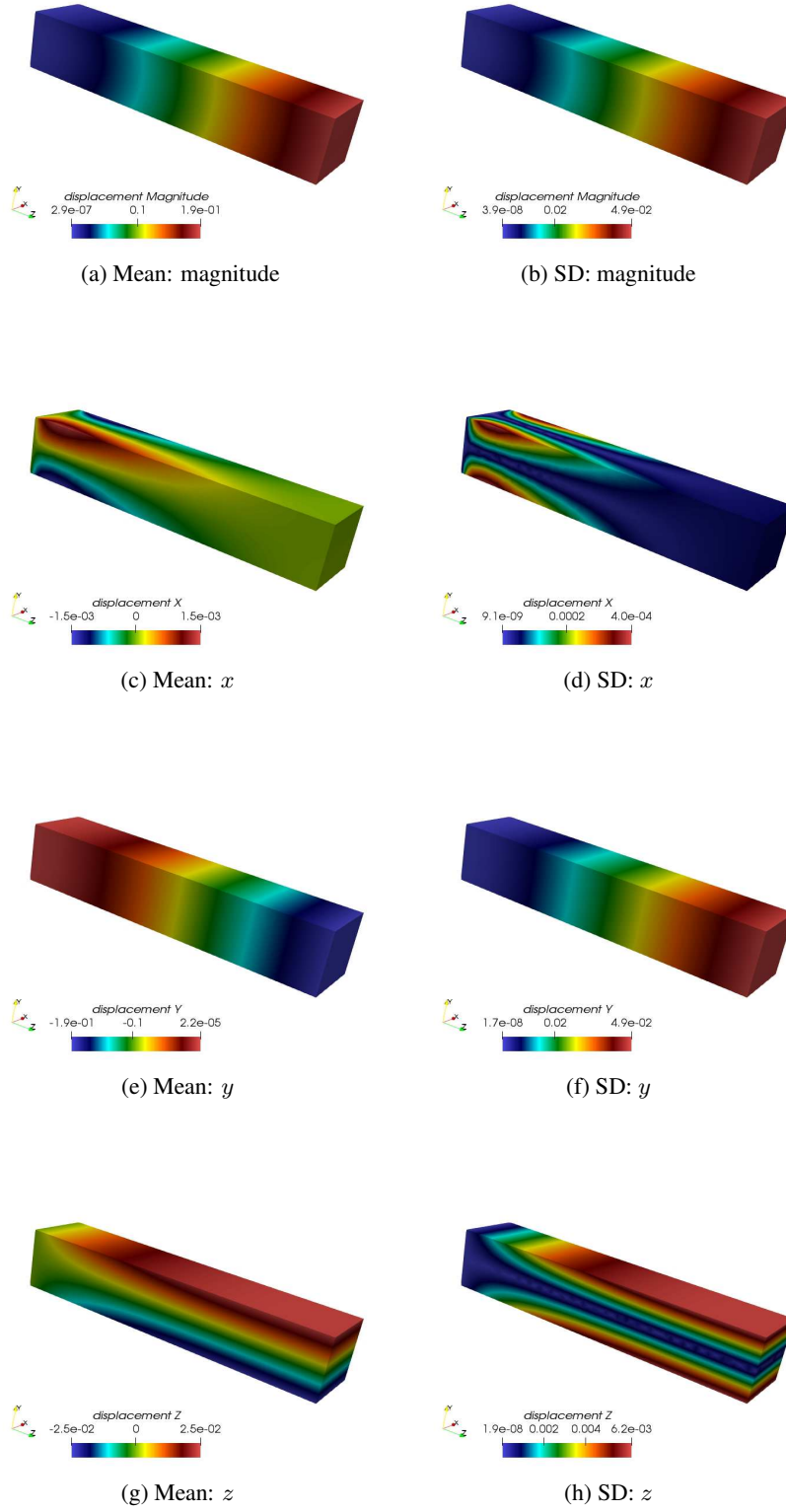


Figure 25: Magnitude and x , y and z components of the mean and standard deviation of the solution process \mathcal{U} .

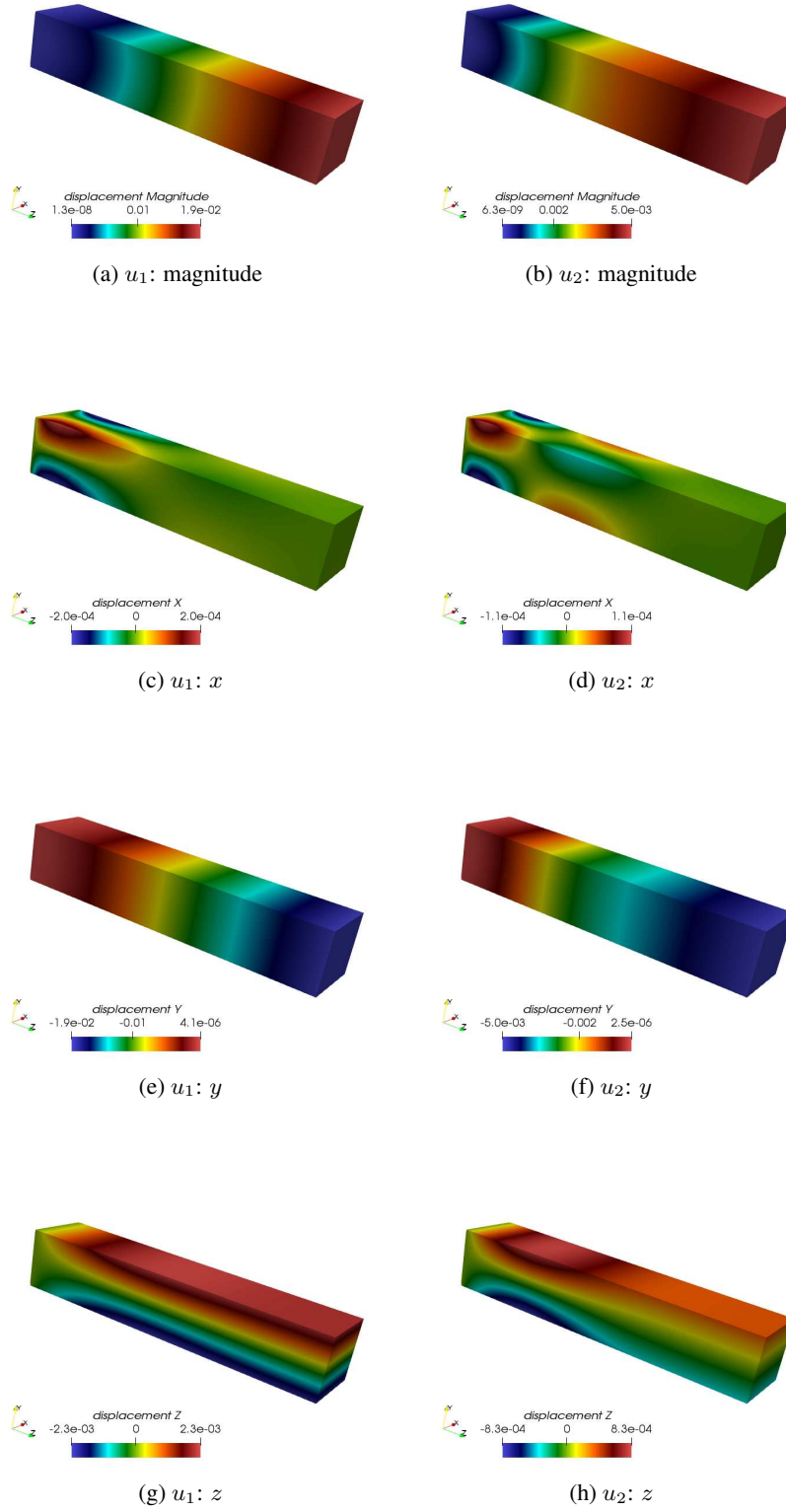


Figure 26: Magnitude and x , y and z components of the selected PCE coefficients of the solution process \mathcal{U} .

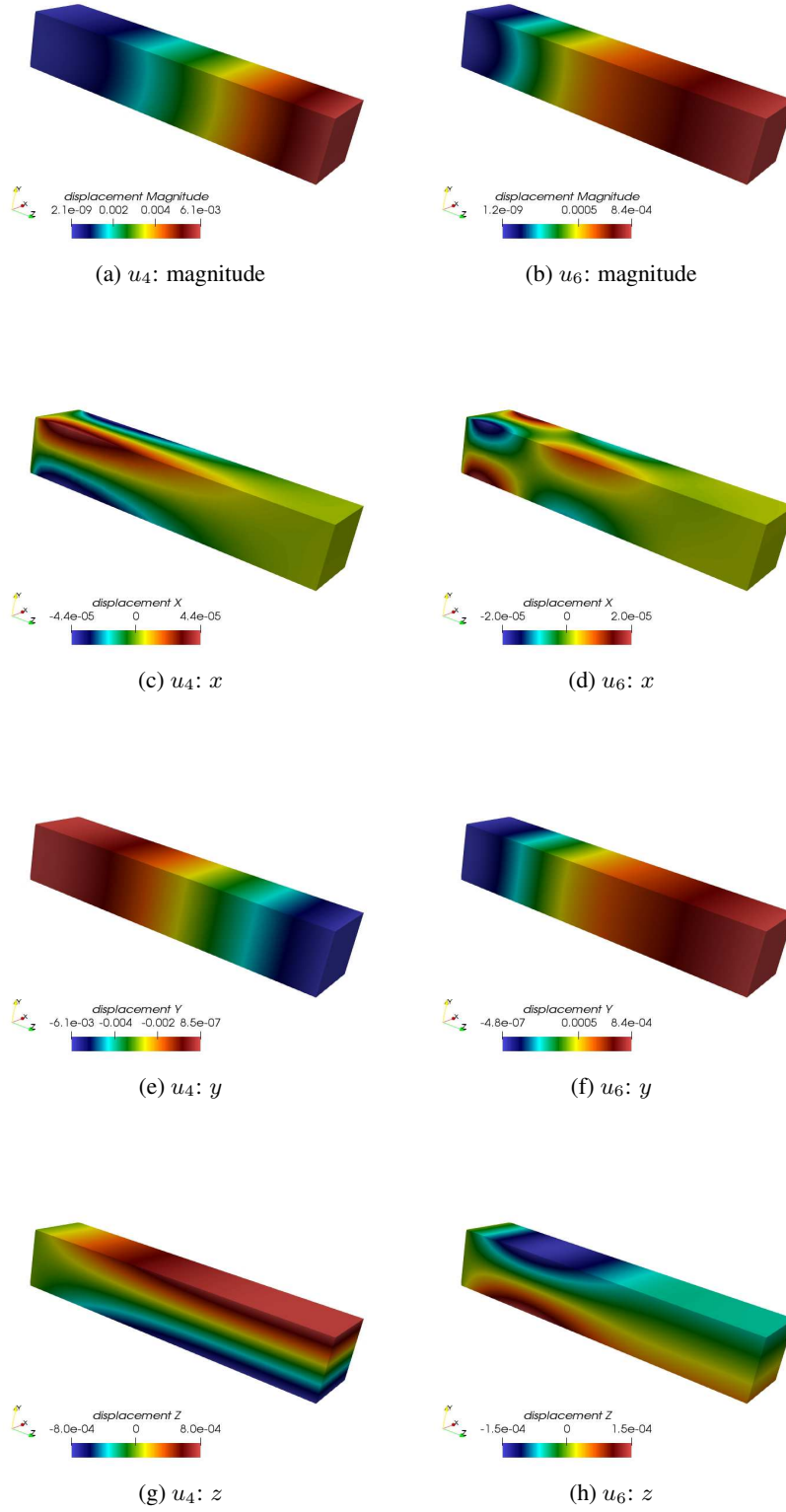


Figure 27: Magnitude and x , y and z components of the selected PCE coefficients of the solution process \mathcal{U} .

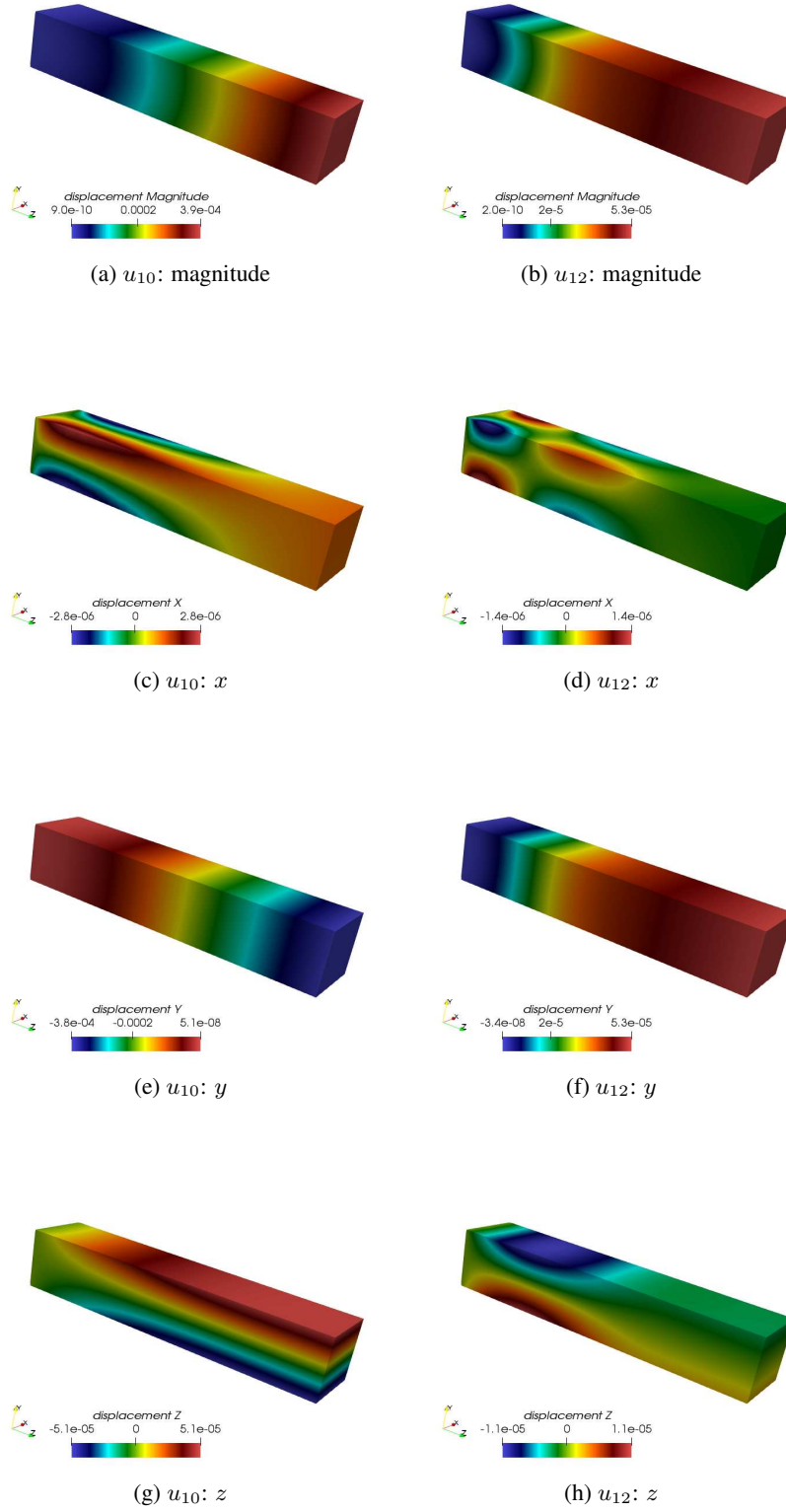


Figure 28: Magnitude and x , y and z components of the selected PCE coefficients of the solution process \mathcal{U} .

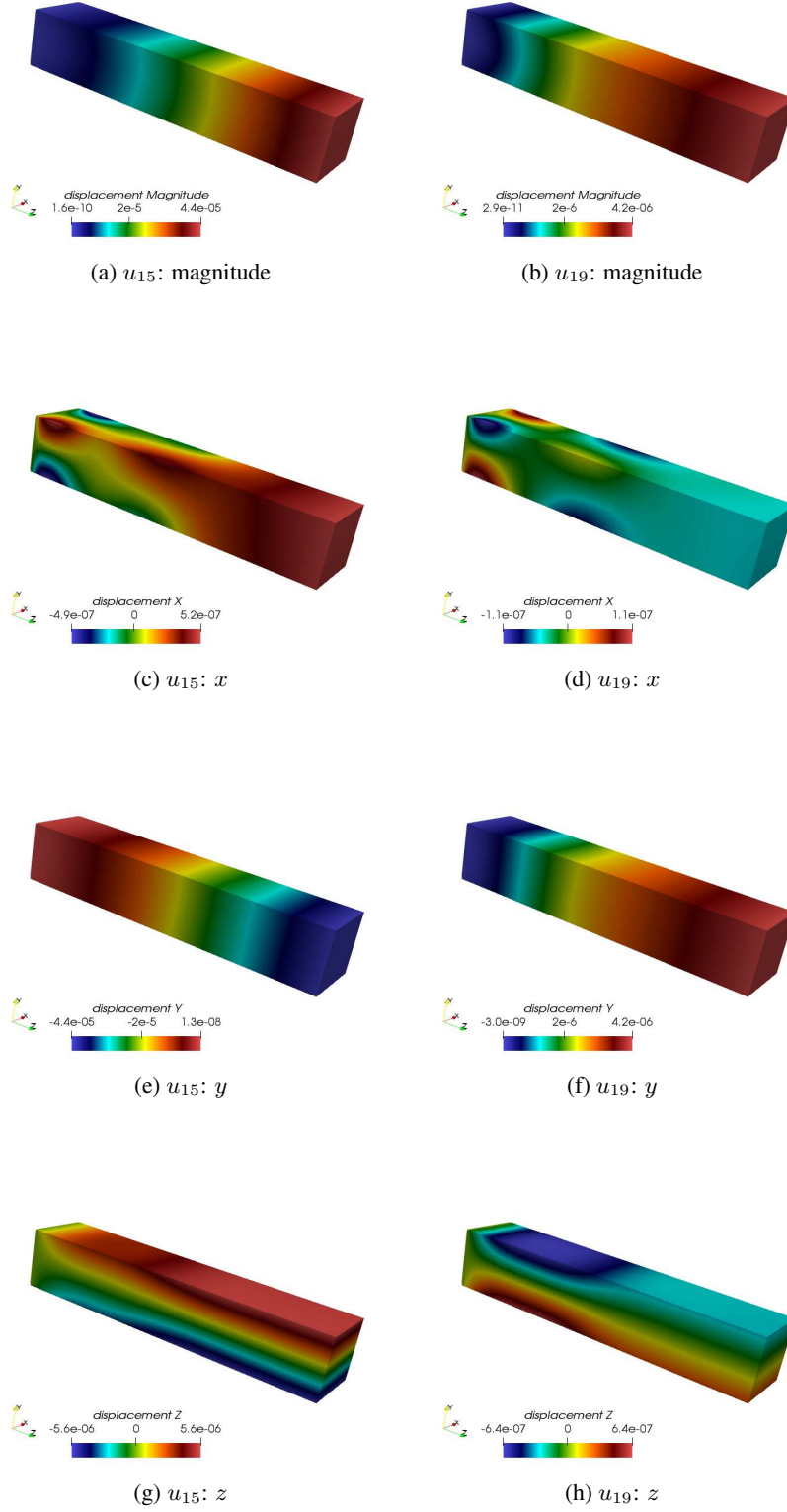


Figure 29: Magnitude and x , y and z components of the selected PCE coefficients of the solution process \mathcal{U} .

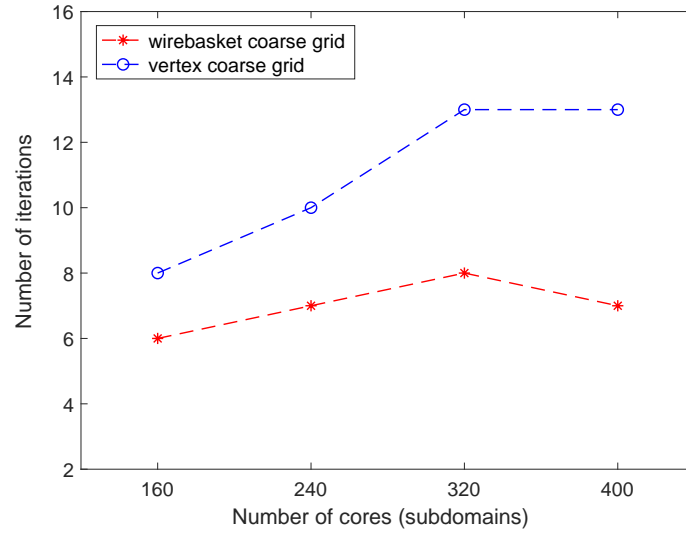


Figure 30: Iteration count versus number of subdomains for the fixed number of PCE terms with fixed mesh resolution.

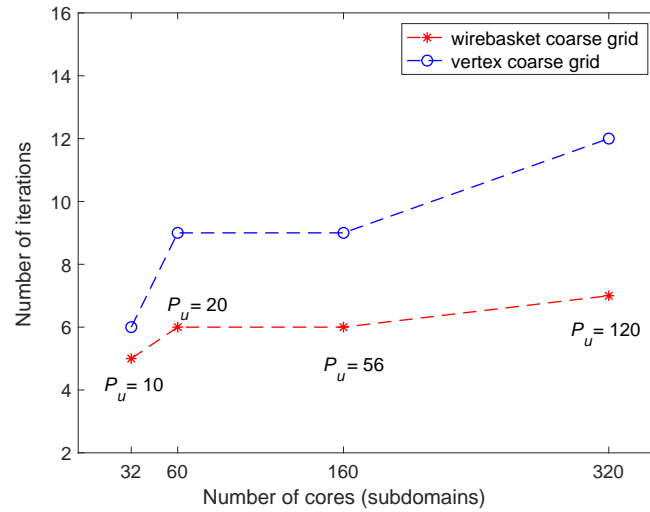


Figure 31: Iteration count versus number of subdomains for the fixed mesh resolution and fixed problem size per subdomain with increasing number of PCEs.

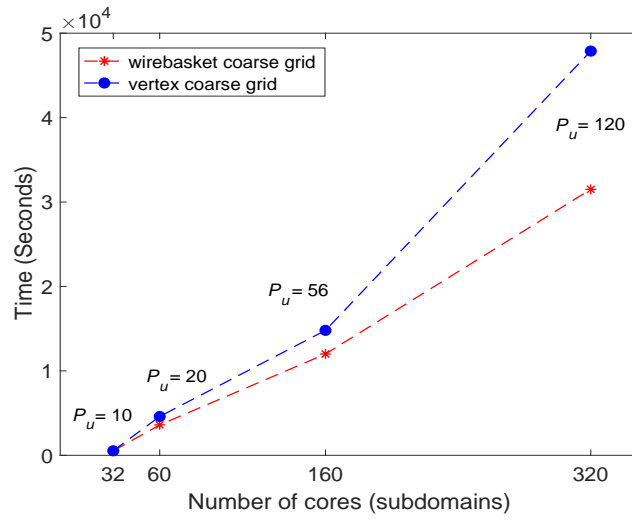


Figure 32: Execution time versus number of subdomains for the fixed mesh resolution and fixed problem size per subdomain with increasing number of PCEs (fixed mesh resolution).

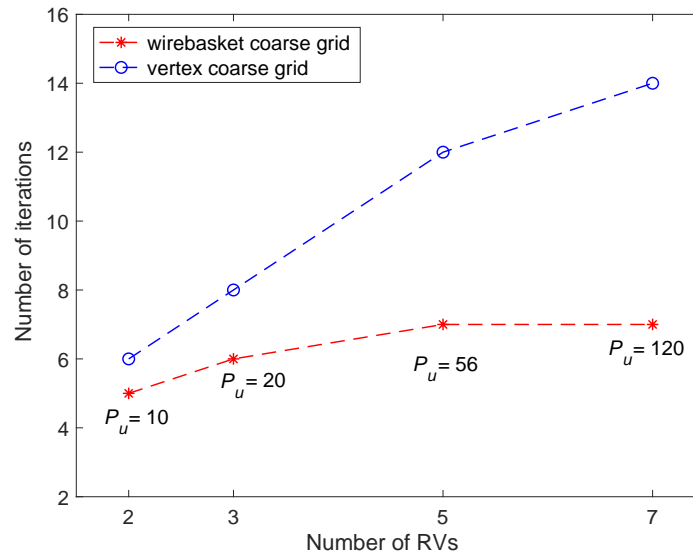


Figure 33: Iteration count versus number of PCE terms for the fixed mesh having fixed number of subdomains.

First, we study the numerical scalability of the solver using PCGM iteration counts (with the tolerance value $tol = 10^{-5}$). Next, the strong and weak parallel scalabilities are investigated using the execution time of the solvers against the number of subdomains. Finally, we present the numerical and parallel scalability plots against the number of random variables and the order of PC expansion.

5.4.1 Numerical Scalability

For a fixed PCE terms ($P_u = 56$) and fixed problem size (48563 nodes and 283886 elements), the PCGM iteration count increases slightly with increasing subdomains, indicating numerical scalability of the wirebasket-based BDD-C/NNC solver (see Fig. 34).

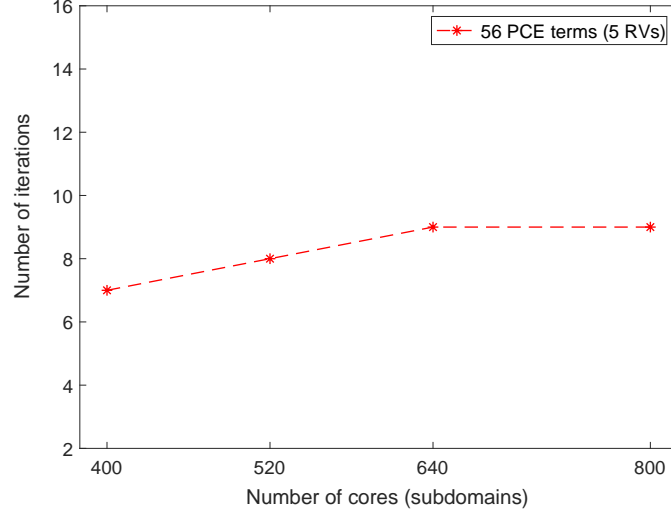


Figure 34: Iteration count versus number of subdomains for the fixed number of PCE terms with fixed mesh resolution.

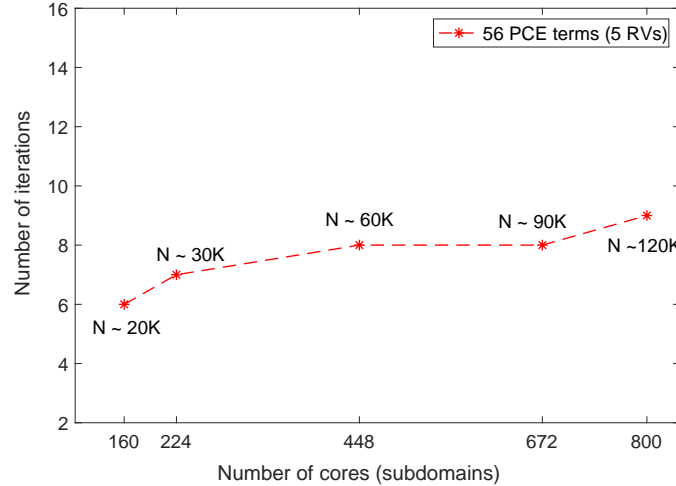


Figure 35: Iteration count versus number of subdomains for the fixed number of PCE terms and the fixed problem size per core with increasing mesh resolution.

Next, for the fixed PCE terms ($P_u = 56$), the global problem size is increased by increasing mesh resolution while keeping a fixed problem size per subdomain (≈ 22500). As shown in Fig. 35, the PCGM iteration count increases

slowly. Fig. 35 demonstrates a reasonable numerical scaling of the wirebasket-based solver against mesh resolution and fixed problem size per subdomains.

5.4.2 Parallel Scalabilities

For a fixed mesh (48563 nodes and 283886 elements) and fixed PCE terms ($P_u = 56$), the execution time reduces with increasing cores as shown in Fig. 36. This fact indicates an excellent strong scaling of the BDDC/NNC solver with the wirebasket based coarse grid.

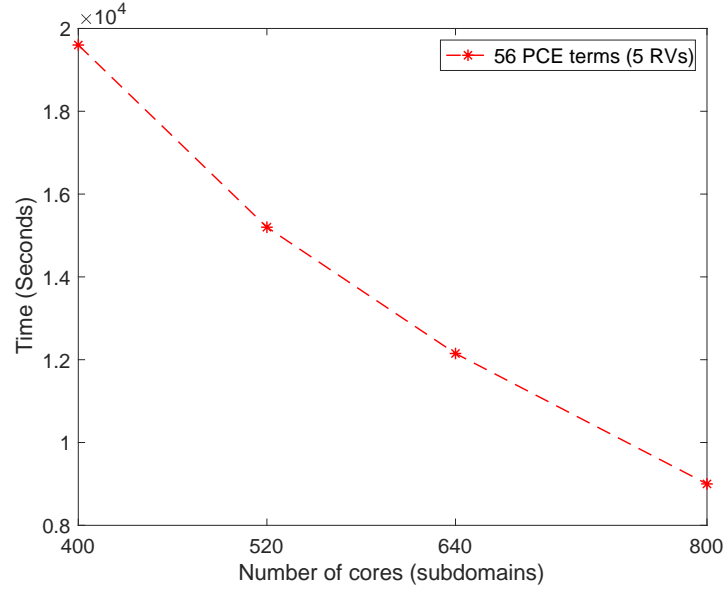


Figure 36: Execution time versus number of subdomains with the number of PCE terms and the fixed mesh resolution.

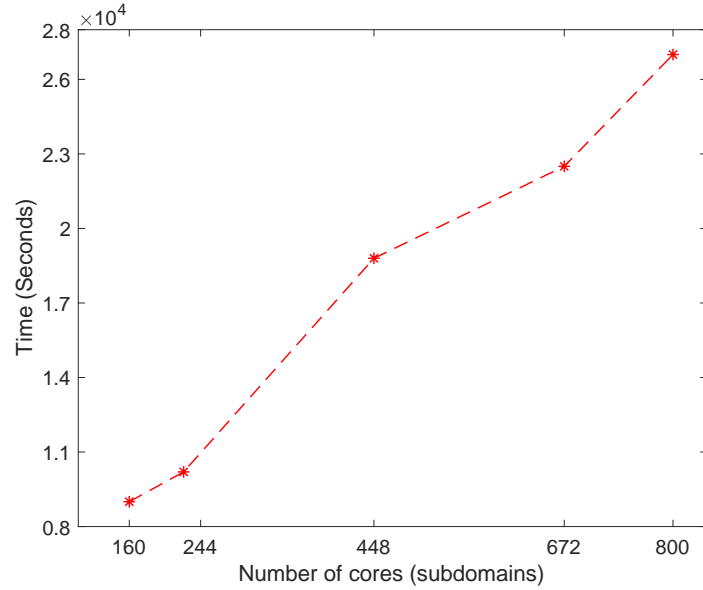


Figure 37: Execution time versus number of subdomains for the fixed number of PCE terms and the fixed problem size per core with increasing mesh resolution.

For a fixed PCE terms ($P_u = 56$), the global problem size is increased by increasing mesh resolution while keeping a fixed problem size per subdomain (≈ 22500); and the corresponding results are shown in Fig. 37. The suboptimal weak scaling is evident in Fig. 37 as the execution time grows with core counts. This is mainly because of the increased parallel overhead with the number of cores caused by the MPI collective communication [4, 5]. Also, in the current case, the global coarse problem size grows quickly with subdomains due to vector-valued solution process. Consequently, the resulting coupled system of equations is computationally challenging. Therefore, it demands significantly more computational efforts compared to that of scalar-valued stochastic PDEs.

5.4.3 Scalability with respect to Stochastic Parameters

In this section, the numerical and parallel scalabilities against stochastic parameters such as the number PCE terms and the order of expansions are presented for a mesh having 48563 nodes and 283886 elements.

The four points in Fig. 38 and 39 represent PCE terms 20, 56, 120 and 220 associated with random variables 3, 5, 7 and 9 respectively. For a fixed mesh with $n_s = 800$ subdomains, increasing PCE terms associated with increasing random variables (with the third-order output PC expansion) lead to a slight variation in the PCGM iteration counts (see Fig. 38). Hence the wirebasket-based solver demonstrates good numerical scaling with increasing random variables.

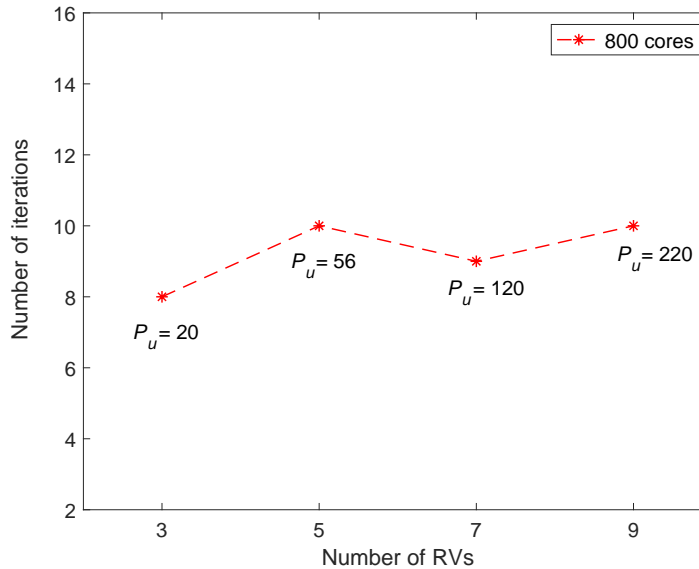


Figure 38: Iteration count versus number of PCE terms for the fixed mesh resolution with fixed number of subdomains.

For a fixed mesh, the global problem size grows with increasing PCE terms. The resulting larger system is tackled using additional cores (by fixing the problem size per core ≈ 18000). The iteration count of the wirebasket based solver against subdomain numbers remains nearly constant (Fig. 39). Hence the wirebasket-based BDDC/NNC-PCGM solver showed acceptable numerical scaling with respect to PCE terms.

For a fixed mesh with $n_s = 800$ subdomains, PCGM iterations grow moderately with increasing PCE orders p_u (with random variables $L = 5$) as shown in Fig. 40. Hence the wirebasket-based solver exhibits satisfactory numerical scaling with respect to the order of PC expansion.

6 Conclusion

In summary, extending the DD preconditioner with a wirebasket-based coarse grid [7, 8, 13, 14] for deterministic PDEs, we formulate a wirebasket-based two-level preconditioner for the stochastic PDEs. The BDDC/NNC solver with the extended wirebasket-based coarse grid is employed to tackle three-dimensional (scalar and vector-valued) stochastic PDEs in high-dimensional stochastic spaces. The novel domain decomposition preconditioner based on the extended wirebasket-based coarse grid is shown to outperform vertex-based coarse grid for stochastic PDEs in three dimensions. The stochastic system matrix assembly procedure can utilize existing deterministic FEM packages and

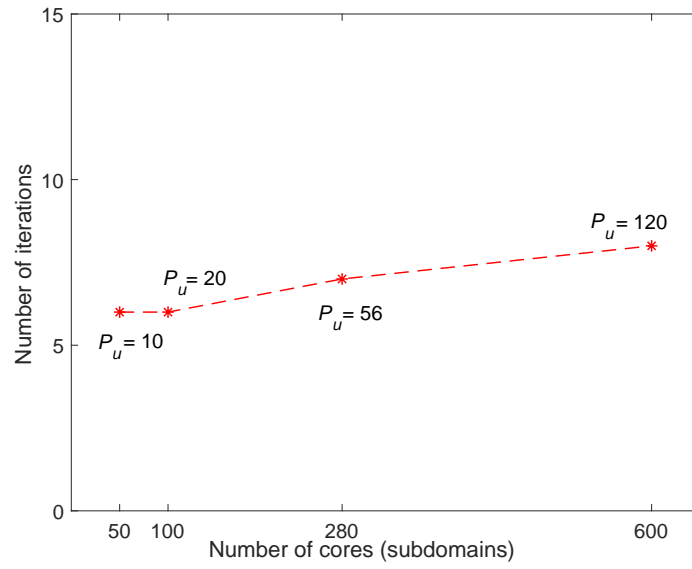


Figure 39: Iteration count versus number of subdomains for increasing number of PCE terms (fixed mesh resolution with the fixed problem size per core).

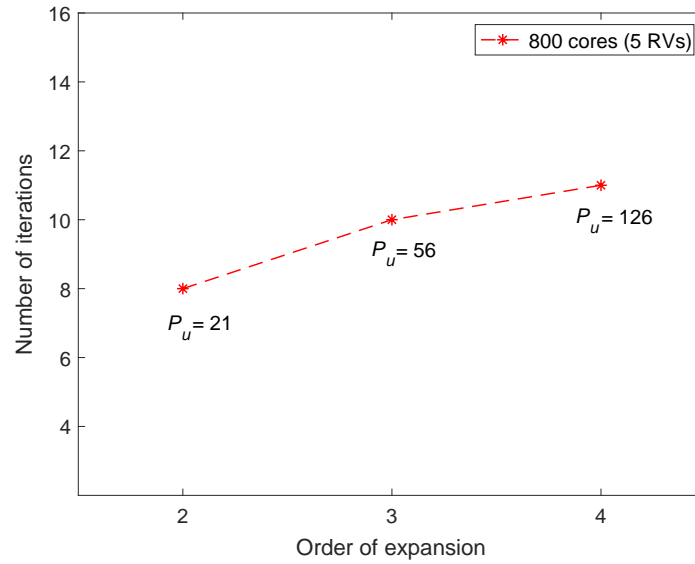


Figure 40: Iteration count versus order of expansion for the fixed mesh resolution with fixed number of subdomains (fixed number of RVs).

thereby reduces the implementational burden of DD-based intrusive SSFEM. Various sparse data structures, routines, iterative solvers and preconditioners are leveraged to tackle the subdomain-level systems. These implementational advances cut execution time and memory usage, and potentially paves the way to tackle extreme-scale uncertainty quantification problems in stochastic PDEs using high performance computing. Numerous simulations are performed to thoroughly investigate the performance of the extended wirebasket-based BDDC/NNC solver to tackle large-scale high-dimensional stochastic PDEs. The numerical and parallel scalings (against subdomain numbers and PCE terms) are essential to understand convergence behavior and utility of domain decomposition solvers for stochastic PDEs.

Although the extended wirebasket based DD preconditioner showed better numerical scaling for the stochastic PDEs illustrated here, the size of the extended coarse problem arising in this setting grows rapidly with (a) the mesh resolution, (b) PCE terms and (c) subdomain numbers. Therefore, the coarse problem solver becomes computational bottleneck in regards to memory requirement and floating point operations. This problem, for instance, can be alleviated by extending the recently proposed algorithms in the deterministic setting which enforces only average constraints over selected edges [41, 42] and may reduce the cost of the coarse problem solver for stochastic PDEs. These aspects are under current investigation.

Acknowledgments

The first author acknowledges the support of an Ontario Trillium scholarship. The fourth author acknowledges the support of the Department of National Defence, Canada and a Discovery Grant from Natural Sciences and Engineering Research Council of Canada. The fifth author acknowledges the support of a Discovery Grant from Natural Sciences and Engineering Research Council of Canada. The computing infrastructure is supported by the Canada Foundation for Innovation (CFI), the Ontario Innovation Trust (OIT), Compute Canada and Calcul Québec.

Sandia National Laboratories is a multimission laboratory managed and operated by National Technology & Engineering Solutions of Sandia, LLC, a wholly owned subsidiary of Honeywell International Inc., for the U.S. Department of Energy's National Nuclear Security Administration under contract DE-NA0003525. This paper describes objective technical results and analysis. Any subjective views or opinions that might be expressed in the paper do not necessarily represent the views of the U.S. Department of Energy or the United States Government.

A Parallel Implementational Details of Domain Decomposition Solvers for SPDEs

The distributed implementation of two-level domain decomposition solvers uses PCGM algorithm [4, 6] with MPI and PETSc libraries [29], as described in Algorithm 1 [4, 6]. The procedure (e.g. [4, 6]) is illustrated for the preconditioned extended Schur complement system below:

$$\mathcal{S}\mathbf{U}_\Gamma = \mathbf{g}_\Gamma, \quad (51)$$

The steps 7 and 13 (in blue) are computationally intensive; hence they need careful implementation. The matrix-vector product and effect of preconditioner on the residual are performed concurrently on each subdomain. Explicit construction of the preconditioner (M^{-1}) and Schur complement matrix (S) are avoided, and Parallel Preconditioning (PP) procedure and Parallel Mat-Vec Product (PMVP) procedure (refer to [6] for more details) are leveraged instead. For large-scale systems (both due to spatial and stochastic resolutions), steps 7 and 13 are critical for minimizing memory requirement and floating-point operations.

The following algorithm outlines the stochastic finite element assembly procedure of a typical block of the subdomain-level matrix defined as:

$$[\mathcal{A}_{\gamma\delta}^s]_{jk} = \sum_{i=0}^{P_A} \langle \psi_i \psi_j \psi_k \rangle \bar{\mathbf{A}}_{\gamma\delta,i}^s, \quad (52)$$

Clearly the memory requirement to assemble and solve the subdomain-level system limits the maximum size of the global problem. For subdomain-level (local) systems, sparse PETSc [29] data structures and solvers are used for effective memory usage in assembly, storage and matrix-vector operations. The local sparse PETSc matrices are stored in compressed row format using PETSc *MatCreateSeqAIJ* routine [29]).

Algorithm 2 outlines the assembly procedure of a typical block of the subdomain-level stiffness matrix, corresponding to Eq. (52) in which stochastic finite element matrix blocks are constructed with deterministic finite element blocks.

Algorithm 1 : Parallel PCGM Algorithm

```

1: Input :  $\mathcal{U}_{\Gamma_0}$ 
2: Initial Residual :  $r_{\Gamma_0} = \mathbf{g}_{\Gamma} - \mathbf{S}\mathcal{U}_{\Gamma_0}$ 
3: Preconditioned Residual :  $z_0 = \mathcal{M}^{-1} r_{\Gamma_0}$ 
4: Compute :  $p_0 = z_0$ 
5: Compute :  $\delta_0 = (r_{\Gamma_0}, z_0)$ 
6: for each iteration,  $i = 0, 1, 2, \dots$ , do
7:   Parallel Mat-Vec Product Procedure :  $q_i = \mathcal{S}p_i$ 
8:   Compute :  $\gamma_i = (q_i, p_i)$ 
9:   Compute :  $\alpha_i = \delta_i / \gamma_i$ 
10:  Update :  $u_{\Gamma_{i+1}} = u_{\Gamma_i} + \alpha_i p_i$ 
11:  Update :  $r_{\Gamma_{i+1}} = r_{\Gamma_i} - \alpha_i q_i$ 
12:  If iteration has converged, Exit
13:  Parallel Preconditioning Procedure :  $z_{i+1} = \mathcal{M}^{-1} r_{\Gamma_{i+1}}$ 
14:  Compute :  $\delta_{i+1} = (r_{\Gamma_{i+1}}, z_{i+1})$ 
15:  Compute :  $\beta_i = \delta_{i+1} / \delta_i$ 
16:  Update :  $p_{i+1} = z_{i+1} + \beta_i p_i$ 
17: end for
18: Output :  $\mathcal{U}_{\Gamma}$ 

```

Algorithm 2 : Stochastic Finite Element Assembly for DD Blocks

```

1: Input : non-zero :  $ijk$  and  $C_{ijk}$ 
2: Create : PETSc-MatCreateSeqAIJ ( $[\mathcal{A}_{\gamma\delta}^s]$ )
3: for  $i = 1, 2, \dots, P_s$  do
4:   Initialize :  $[\bar{\mathcal{A}}_{\gamma\delta,i}^s]_i$ 
5:   Call : Deterministic Finite Element Matrix Assembly ( $[\bar{\mathcal{A}}_{\gamma\delta,i}^s]_i$ )
6:   for  $j = 1, 2, \dots, P_u$  do
7:     for  $k = 1, 2, \dots, P_u$  do
8:       if ( $i, j, k == \text{nonZero}(ijk)$ ) then
9:         Insert : call PETSc-MatSetValues ( $\{C_{ijk} \times [\bar{\mathcal{A}}_{\gamma\delta,i}^s]_i\} \Rightarrow [\mathcal{A}_{\gamma\delta}^s]$ )
10:      end if
11:    end for
12:  end for
13:  Destroy :  $[\bar{\mathcal{A}}_{\gamma\delta,i}^s]_i$ 
14: end for
15: Output :  $[\mathcal{A}_{\gamma\delta}^s]$ 

```

The PETSc *Mat* sparse data structure is used for efficient memory usage. For effective memory reuse (e.g. in handling a large number of random variables), the deterministic matrix blocks are destroyed after completing the stochastic finite element matrix assembly.

References

- [1] Abhijit Sarkar, Nabil Benabbou, and Roger Ghanem. Domain decomposition of stochastic PDEs: theoretical formulations. *International Journal for Numerical Methods in Engineering*, 77(5):689–701, 2009.
- [2] Waad Subber and Abhijit Sarkar. A domain decomposition method of stochastic PDEs: An iterative solution techniques using a two-level scalable preconditioner. *Journal of Computational Physics*, 257:298–317, 2014.
- [3] Waad Subber and Abhijit Sarkar. Dual-primal domain decomposition method for uncertainty quantification. *Computer Methods in Applied Mechanics and Engineering*, 266:112–124, 2013.
- [4] Waad Subber. *Domain decomposition methods for uncertainty quantification*. PhD thesis, Carleton University Ottawa, 2012.
- [5] Ajit Desai, Mohammad Khalil, Chris Pettit, Dominique Poirel, and Abhijit Sarkar. Scalable domain decomposition solvers for stochastic PDEs in high performance computing. *Computer Methods in Applied Mechanics and Engineering*, 335:194–222, 2017.

- [6] Ajit Desai. *Scalable Domain Decomposition Algorithms for Uncertainty Quantification in High Performance Computing*. PhD thesis, Carleton University, 2019.
- [7] James H Bramble, Joseph E Pasciak, and Alfred H Schatz. The construction of preconditioners for elliptic problems by substructuring. iv. *Mathematics of Computation*, 53(187):1–24, 1989.
- [8] Barry F Smith. A domain decomposition algorithm for elliptic problems in three dimensions. *Numerische Mathematik*, 60(1):219–234, 1991.
- [9] Barry Smith, Petter Bjorstad, and William Gropp. *Domain decomposition: parallel multilevel methods for elliptic partial differential equations*. Cambridge University Press, 2004.
- [10] Andrea Toselli and Olof Widlund. *Domain decomposition methods: algorithms and theory*, volume 34. Springer, 2005.
- [11] Barry F Smith. An optimal domain decomposition preconditioner for the finite element solution of linear elasticity problems. *SIAM Journal on Scientific and Statistical Computing*, 13(1):364–378, 1992.
- [12] Debraj Ghosh, Philip Avery, and Charbel Farhat. A FETI-preconditioned conjugate gradient method for large-scale stochastic finite element problems. *International Journal for Numerical Methods in Engineering*, 80(6-7):914–931, 2009.
- [13] Maksymilian Dryja and Olof B Widlund. Some domain decomposition algorithms for elliptic problems. In *Iterative methods for large linear systems*, pages 273–291. Elsevier, 1990.
- [14] Jan Mandel. Two-level domain decomposition preconditioning for the p-version finite element method in three dimensions. *International Journal for Numerical Methods in Engineering*, 29(5):1095–1108, 1990.
- [15] Jan Mandel. Iterative solvers by substructuring for the p-version finite element method. *Computer Methods in Applied Mechanics and Engineering*, 80(1-3):117–128, 1990.
- [16] Anders Logg, Andre Mardal, and Garth Wells. *Automated solution of differential equations by the finite element method: The FEniCS book*, volume 84. Springer Science & Business Media, 2012.
- [17] Anders Logg, Garth Wells, and Johan Hake. DOLFIN: A C++/Python finite element library. In *Automated Solution of Differential Equations by the Finite Element Method*. Springer, 2012.
- [18] Olivier Le Maître and Omar M Knio. *Spectral methods for uncertainty quantification: with applications to computational fluid dynamics*. Springer Science & Business Media, 2010.
- [19] MS Eldred and John Burkardt. Comparison of non-intrusive polynomial chaos and stochastic collocation methods for uncertainty quantification. *AIAA paper*, 976:1–20, 2009.
- [20] Matthew Reagan, Habib Najm, Roger Ghanem, and Omar Knio. Uncertainty quantification in reacting-flow simulations through non-intrusive spectral projection. *Combustion and Flame*, 132(3):545–555, 2003.
- [21] Graham-cedar: New national heterogeneous HPC clusters managed by Compute Canada, 2017.
- [22] David E Keyes and William D Gropp. A comparison of domain decomposition techniques for elliptic partial differential equations and their parallel implementation. *SIAM Journal on Scientific and Statistical Computing*, 8(2):s166–s202, 1987.
- [23] Roger Ghanem. Ingredients for a general purpose stochastic finite elements implementation. *Computer Methods in Applied Mechanics and Engineering*, 168(1):19–34, 1999.
- [24] Roger Ghanem and Pol Spanos. *Stochastic finite elements: a spectral approach*. Springer-Verlag, New York, 1991.
- [25] Ajit Desai and Sunetra Sarkar. Analysis of a nonlinear aeroelastic system with parametric uncertainties using polynomial chaos expansion. *Mathematical Problems in Engineering*, 2010, 2010.
- [26] Tarek Mathew. *Domain decomposition methods for the numerical solution of partial differential equations*, volume 61. Springer Science & Business Media, 2008.
- [27] Patrick Billingsley. *Probability and measure*. John Wiley & Sons, 2008.
- [28] William Gropp, Ewing Lusk, and Anthony Skjellum. *Using MPI: portable parallel programming with the message-passing interface*, volume 1. MIT press, 1999.
- [29] Satish Balay, Shrirang Abhyankar, Mark Adams, Jed Brown, Peter Brune, Kris Buschelman, Lisandro Dalcin, Victor Eijkhout, William Gropp, Dinesh Kaushik, Matthew Knepley, Dave May, Lois McInnes, Karl Rupp, Patrick Sanan, and Barry Smith. PETSc users manual 3.7. Technical report, Argonne National Laboratory, 2017.

-
- [30] Christophe Geuzaine and François Remacle. GMSH: A 3-D finite element mesh generator with built-in pre- and post-processing facilities. *International Journal for Numerical Methods in Engineering*, 79(11):1309–1331, 2009.
 - [31] GMSH- a three-dimensional finite element mesh generator, 2017.
 - [32] George Karypis and Vipin Kumar. METIS–unstructured graph partitioning and sparse matrix ordering system, version 2.0, 1995.
 - [33] METIS- serial graph partitioning, 2017.
 - [34] Bert Debusschere, Khachik Sargsyan, and Cosmin Safta. UQTK version 2.1 user manual. Technical report, Sandia National Laboratory (SNL), 2013.
 - [35] James Ahrens, Berk Geveci, and Charles Law. ParaView: An end-user tool for large-data visualization, 2005.
 - [36] ParaView- multi-platform data analysis and visualization application, 2017.
 - [37] The Mathworks Inc: Matlab user’s guide, 2015.
 - [38] Niagara supercomputer: New national homogeneous HPC clusters managed by Compute Canada, 2018.
 - [39] Alireza Doostan, Roger G Ghanem, and John Red-Horse. Stochastic model reduction for chaos representations. *Computer Methods in Applied Mechanics and Engineering*, 196(37-40):3951–3966, 2007.
 - [40] Roger G Ghanem, Alireza Doostan, and John Red-Horse. A probabilistic construction of model validation. *Computer Methods in Applied Mechanics and Engineering*, 197(29-32):2585–2595, 2008.
 - [41] Axel Klawonn and Olof B Widlund. Dual-primal FETI methods for linear elasticity. *Communications on Pure and Applied Mathematics: A Journal Issued by the Courant Institute of Mathematical Sciences*, 59(11):1523–1572, 2006.
 - [42] Axel Klawonn and Oliver Rheinbach. A parallel implementation of dual-primal FETI methods for three-dimensional linear elasticity using a transformation of basis. *SIAM Journal on Scientific Computing*, 28(5):1886–1906, 2006.